MODELING WIRE ANTENNAS

Wire antennas represent the oldest category of antenna types, dating back to the successful transatlantic transmissions by Marconi and even before that to the theoretical and experimental efforts of Hertz, Maxwell, and others. In 1898, Pocklington developed an integral equation for a dipole antenna whose numerical solution remained relatively intractable until the digital computer made its numerical solution possible. This integral equation, and its various generalizations, provide the starting point for essentially all wire-antenna numerical modeling now routinely done and on which the discussion below focuses. The emphasis here is on describing and demonstrating the capabilities of wire-antenna models rather than on cataloging a large number of antenna types and characteristics, because the extremely large variety of the latter is incompatible with the space available and the scope of the discussion.

Because our primary goal here is to summarize the modeling and use of wire antennas rather than to concentrate on their numerical modeling alone, we consider only the Pocklington form of the types of integral equations available for wire-antenna analysis and design, although several others are included for reference (1). The numerical approaches described are rather general, and specific details are summarized as implemented in two computer codes. One is Numerical Electromagnetics Code (NEC) (2) and the other is Thin-Wire Time Domain (TWTD) (3). The former is a widely used frequency-domain model, and the latter is its time-domain counterpart. Both were developed at Lawrence Livermore National Laboratory, and versions of both are in the public domain.

PRELIMINARIES

Integral Equations and Wire Modeling

The derivation of an integral equation for a perfect electric conductor (PEC) is approached in various ways, but perhaps the most physically appealing is to begin with Maxwell's equations written in their source-integral form whose kernel is a Green's function for an electric source in an infinite medium. The source integral gives the secondary field (also called induced, scattered, or radiated field) caused by a current on the body flowing in response to a primary field (also called incident, applied, or exciting field). By expressing the secondary field over loci of points where the behavior of the total field (applied plus radiated) is known via boundary or continuity conditions, an integral equation for the induced source is obtained.

Two broad general classes of integral equations are encountered, depending on whether the unknown source occurs only under the integral (a first-kind Fredholm integral equation) or also outside of it (a second-kind integral equation) (4). In electromagnetics, a first-kind integral equation arises when the forcing function (primary field) is an electric field, and a second-kind integral equation arises when the forcing function is a magnetic field. Although it is usual for derivatives of the unknown also to occur, the resulting equation is commonly called an integral equation (IE), rather than an integro-differential equation as would be strictly correct.

Generally speaking, a magnetic-field IE (MFIE) is best suited for smooth, closed objects, and it is analytically inapplicable to objects thin in one dimension, such as plates, shell-like structures, and wires. The electric-field IE (EFIE) is not limited by these constraints, and so becomes the only practical type for modeling the wires of interest here. Because of anomalous internal resonances, both the MFIE and the EFIE fail numerically near certain discrete frequencies, and a combined-field IE (CFIE) comprised of their sum is needed for modeling smooth, closed objects.

At its simplest, a wire is a PEC of constant, circular cross section whose circumference in wavelengths C is no greater than 1 so that its radius in wavelengths, $a = C/2\pi$, although it is usual to employ a maximum radius only a tenth or so as large. By definition, to be an *"electromagnetic"* wire, it must satisfy at least two conditions: (1) the effect of any circumferential or azimuthal current (one that flows on the wire surface in a direction normal to its axis) is negligible; and (2) the longitudinal current (the surface current flowing along its axis) is independent of the azimuth angle, that is, it is uniform around the circumference.

A further requirement also usually imposed for analytical and numerical convenience is that the thin-wire (or reduced-kernel) approximation is employed, so that the two-dimensional surface integration required to evaluate the fields of

sources on a general surface is approximated by a line integral along the wire's axis. This is discussed later.

Most wire modeling, even when approximating a closed surface by a wire mesh or grid, is done with piecewise linear (straight) segments. Because meshes used as approximations to curvilinear surfaces cannot be made of planar square or rectangular elements, this means that junctions of wires meeting at variable angles are encountered. Although requirement (2) above is then almost certainly violated, the thin-wire approximation remains accurate enough to produce useful results. The added difficulty of including such higher-order effects as a circumferentially nonuniform longitudinal current is evidently not commensurate with the improvement that might be realized. Use of straight segments is also common in modeling such simple objects as circular loops, helices, conical spirals, etc.

Guidelines have been developed over the years to help users of wire codes choose modeling parameters more likely to lead to acceptable results. For example, when modeling circular loops, the centerline circumference of the polygonal approximation should equal the circumference of the actual loop and a minimum of six wire segments must be used to model the loop in the vicinity of its first resonance, that is, where $C \sim 1$. This relates to the fact that experience has shown that nominally six wire segments per wavelength are needed to achieve acceptable accuracy, when the sampling density of the unknown current is *"wavelength-driven."* When more segments are needed to properly represent the geometry of the object being modeled, the required segment lengths are required to be much smaller, and the sampling density is *geometry*-driven." When approximating a solid surface with a wire mesh as shown in Fig. 1, the maximum mesh openings are no greater than 0.1 wavelength on a side. The radius of the mesh wires also needs to be such that their total area is twice that of the surface they represent, so that the wire area in each direction of a local, orthogonal coordinate system approximates that of the surface being modeled (6), the *"equal-area"* rule. A computed result showing that the front-to-back ratio of a backscreen of parallel wires is maximized when the equal-area rule is satisfied is shown in Fig. 2 (5). Modeling guidelines for wire antennas are discussed in more detail elsewhere (6).

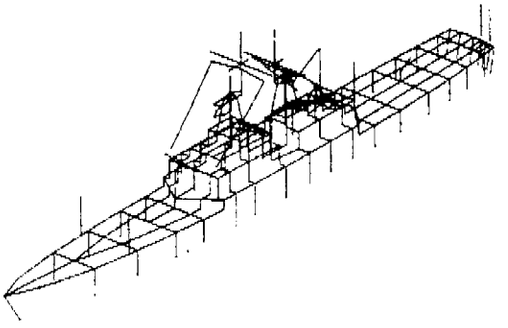

Figure 1. This wire-grid model of a ship (7) is intended for the HF band and lower, where the length of the grid wires is less than 0.1 wavelength and has more than 829 segments. Because the ship is in salt water, which becomes a perfectly conducting half-space to which all of the wires forming its lower sides are connected, the model is not closed on the bottom. Wire-grid models with thousands of segments have been used.

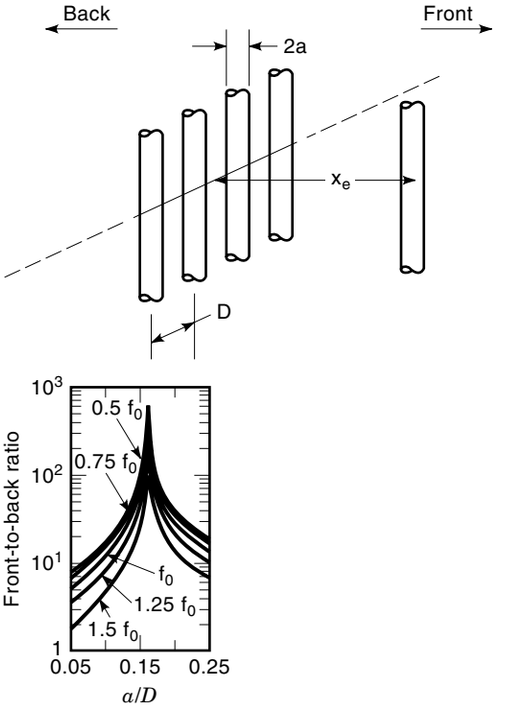

Figure 2. This two-dimensional backscreen model, consisting of equally spaced, infinite wires with an excited element in front, was studied parametrically to determine the wire radius with the largest front-to-back ratio (FBR) to gain insight about modeling a continuous surface with wires (5). For a 50-wire backscreen, $a = 2\pi D$ provides the maximum FBR, where the wire and a continuous backscreen have equal areas over a 3 : 1 frequency range.

Finally, it should be recognized that a wire model is not limited to circular PECs. A thin-wire model can be used for literally any object that satisfies condition (1) previously stated. Its cross section can vary from a flat strip to an arbitrarily irregular shape. For a flat strip of width w, an equivalent radius is found to be $a = w/2$. Other simple cross sections, such as triangular, are also amenable to thin-wire modeling, where the radius of the equivalent circular wire is established from simple formulas by quasi-static analysis (8).

IMPORTANT PROPERTIES OF WIRE ANTENNAS

The purpose of the analytical treatment and its implementation to develop a numerical model, described later, is to assess the performance characteristics of antennas of interest, of which some of the more important are described here (1).

Input Impedance and Admittance. The input impedance Z_{in}, of an antenna is needed to match an antenna to its source

and is also an important quantity in determining its efficiency, defined as

$$\eta = P_{\text{rad}}/(P_{\text{rad}} + P_{\text{loss}}) = P_{\text{rad}}/P_{\text{in}} \tag{1}$$

where P_{rad} and P_{loss} are the radiated powers and P_{loss} arises from the losses to which the antenna is subject. From a numerical and analytical perspective, the antenna's admittance Y_{in} is normally the more accurately obtainable quantity, because the real conductance G_{in} is determined wholly by P_{in}, whereas the reactive susceptance B_{in} is very sensitive to feed-region geometry (discussed later). The real and reactive components of the impedance, on the other hand, which is simply the inverse of the admittance, is affected by whatever errors arise in the susceptance. Furthermore, when there are no losses, it is straightforward to obtain the conductance by simply integrating the far-field power flow, a quantity that is also relatively insensitive to errors in the computed current distribution. By contrast, the susceptance requires an accurate solution of the antenna's near fields, because it is related to the stored power that they represent.

The admittance is defined as

$$Y_{\text{in}} = I(s_{\text{in}})/V(s_{\text{in}}) = I_{\text{in}}/V_{\text{in}} = 1/Z_{\text{in}} \tag{2}$$

where s_{in} is the place at which the driving voltage V_{in} is applied and I_{in} is the current there. Determining a realistic value of V_{in} from a numerical model presents a problem because it is sensitive to the way the feed region is described and it is difficult to replicate the physical arrangement with good fidelity. Feedpoint-modeling errors affect both G_{in} and B_{in} though uncertainty in V_{in} is sometimes resolved, as far as its effect on G_{in} is concerned, by far-field integration. In a computer code like NEC that uses point matching where it is assumed that $V_{\text{in}} = -E_{\text{in}}\Delta$, with Δ the length of the feed segment (see section later on numerical implementation), this uncertainty is usually resolved by integrating $E_{\tan}$ in the vicinity of the feedpoint.

The Far-Field and Radiated Power. The power radiated by an antenna is usually determined by integrating the far-field power flow over a closed surface containing the antenna as given by

$$P_{\text{rad}} = \frac{1}{2}\text{Re}\left[\int\int_{\text{S}} \mathbf{E}\times\mathbf{H}^*\cdot d\mathbf{s}\right] \equiv \frac{1}{2}I_{\text{in}}^2 R_{\text{rad}} \tag{3a}$$

where S is the enclosing surface, usually a sphere centered on a convenient part of the antenna, Re denotes the real part, $d\mathbf{s}$ has a unit normal in the outward direction, $\mathbf{E}$ and $\mathbf{H}$ are the peak values of the fields and R_{rad} is the radiation resistance. The input power equals P_{rad} unless there are losses, in which case it is found from

$$P_{\text{in}} = \frac{1}{2}\text{Re}(V_{\text{in}}I_{\text{in}}^*) \tag{3b}$$

Directivity and Gain. The directive gain of an antenna $G_{\text{D}}(\theta, \varphi)$ is defined as the ratio of real-power flux density in the far field in the direction (θ, φ) to its average value over S, so that

$$\begin{aligned} G_{\text{D}}(\theta,\varphi) &= \frac{\text{Re}[(\mathbf{E}\times\mathbf{H}^*)\cdot\hat{\mathbf{r}}]}{\lim\limits_{r\to\infty}\left[\left(\dfrac{1}{4\pi r^2}\right)Re\int\int_S(\mathbf{E}\times\mathbf{H}^*)\cdot\hat{\mathbf{r}}d\mathbf{s}\right]} \\ &= 2\pi r^2\frac{\text{Re}[(\mathbf{E}\times\mathbf{H}^*)\cdot\hat{\mathbf{r}}]}{P_{\text{rad}}} \end{aligned} \tag{4a}$$

where $P_{\text{rad}}/(4\pi r^2)$ is equivalent to the power density of an isotropic antenna radiating the power P_{rad}. The directivity D of an antenna is defined as the maximum value of the directive gain, or

$$D = \max\{G_{\text{D}}(\theta,\varphi)\} \tag{4b}$$

and finally the gain is defined as in Eq. (4a) but including the losses so that

$$G(\theta,\varphi) = 2\pi r^2\frac{\text{Re}[(\mathbf{E}\times\mathbf{H}^*)\cdot\hat{\mathbf{r}}]}{P_{\text{in}}} = \eta G_{\text{D}}(\theta,\varphi) \tag{4c}$$

A Summary of Analytical Results for Some Common Antennas

Although the complexity of real antennas located in their actual environments precludes analytical solutions, and necessitates numerical models like those previously discussed, a wide variety of simple antennas have been studied over the years. Some important properties of a large number of these antennas are summarized for ready reference in Table 1 (1,9).

NUMERICAL MODELING OF ANTENNAS

Although attention here addresses specifically only the numerical treatment of the Pocklington-type IE, for completeness, several different types of thin-wire IEs are included in Table 2 (1). These are all frequency-domain IEs, because most wire modeling uses that approach, but a brief review of wire time-domain modeling concludes this section.

As a starting point, we include the EFIE and MFIE for smooth surfaces from which such equations can be derived (1):

$$\hat{\mathbf{n}}\times\mathbf{E}^{\text{i}}(\mathbf{r}) = -\hat{\mathbf{n}}\times\left[\frac{1}{4\pi j\omega\epsilon_\infty}\int_{\text{S}}\mathbf{J}_{\text{S}}(\mathbf{r})\cdot\overrightarrow{\overrightarrow{\mathbf{G}}}_\infty(\mathbf{r},\mathbf{r}')d^2r'\right] \tag{5}$$

and

$$\mathbf{J}_{\text{S}}(\mathbf{r}) = 2\hat{\mathbf{n}}\times\mathbf{H}^{\text{i}}(\mathbf{r}) + \frac{1}{2\pi}\int_{\text{S}}\mathbf{J}_{\text{S}}(\mathbf{r}')\cdot\overrightarrow{\overrightarrow{\Gamma}}_\infty(\mathbf{r},\mathbf{r}')d^2r' \tag{6}$$

where

$$\begin{aligned} \overrightarrow{\overrightarrow{\mathbf{G}}}_\infty(\mathbf{r},\mathbf{r}') &= (\nabla\nabla + k_\infty^2)g_\infty(R) \\ \overrightarrow{\overrightarrow{\Gamma}}_\infty(\mathbf{r},\mathbf{r}') &= \overrightarrow{\overrightarrow{\mathbf{I}}}\times\nabla' g_\infty(R) \end{aligned} \tag{7}$$

Equation (1) is the EFIE and Eq. (2) is the MFIE, where the unknown surface-current density is $\mathbf{J}_{\text{s}}(\mathbf{r})$, $\hat{\mathbf{n}}$ is an outward-

Table 1. Properties of Some Simple Antennas

Type	Configuration	Impedance: Resistive at f_r·9 $R(\Omega)$	–3-dB Bandwidth Percent	Gain: dB above Isotropic	Gain: dB above Dipole	Polarization	Pattern number
Isotropic radiator (theoretical)	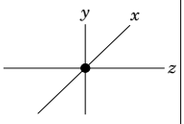	–	–	0	–2.14	none	A
Small dipole $L > \lambda/2$	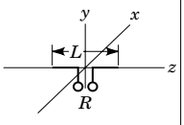	–	–	1.74	–0.4	h	B
Thin dipole $L = \lambda/2$ $L/D = 276$	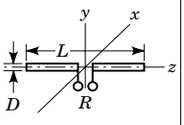	60	34	2.14	0	h	B
Thick dipole $L = \lambda/2$ $L/D = 51$	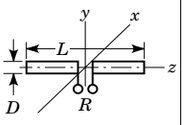	49	55	2.14	0	h	B
Cylindrical dipole $L = \lambda/2$ $L/D = 10$	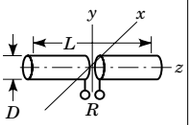	37	100	2.14	0	h	B
Cylidrical dipole $L = \lambda$ $L/D = 9.6$	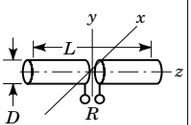	150	130	3.64	1.5	h	B

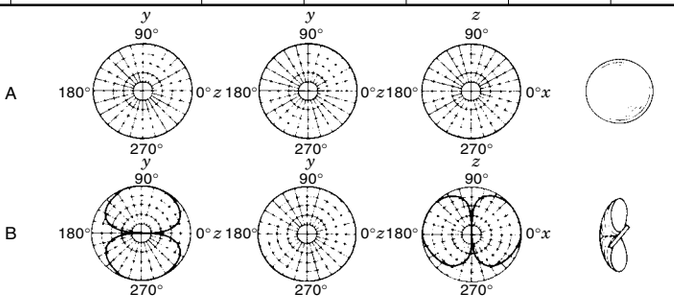

pointing, surface-normal, unit vector and the other quantities are defined in Table 2. The quantities $\vec{\vec{G}}_\infty(\mathbf{r}, \mathbf{r}')$ and $\vec{\vec{\Gamma}}_\infty(\mathbf{r}, \mathbf{r}')$ are known as Green's dyads for the electric and magnetic fields of electric current sources.

It should be understood that $C(\mathbf{r})$ in the equations of Table 2 represents the geometrical configuration of the wire or collection of wires to be modeled and, therefore, does not need to be spatially continuous. The subscript "∞" is used on various quantities in the table to emphasize their association with an infinite medium, as we next consider the half-space problem.

Extension of the previous infinite-medium IEs is straightforward for a perfectly conducting half-space, a common starting point for treating imperfectly conducting or electromagnetically penetrable grounds, an especially important application of wire-antenna modeling. By convention, the half-space occupies the region $z \leq 0$. It can be deduced that (1), because an object located above a PEC half-space is electromagnetically "imaged" or mirrored in it, the vertical components of the image electric currents flow in the same direction as the actual currents and the horizontal components are

Table 1. *(Continued)*

Type	Configuration	Impedance: Resistive at f_r·9 $R(\Omega)$	–3-dB Bandwidth Percent	Gain: dB above Isotropic	Gain: dB above Dipole	Polarization	Pattern number
Folded dipole $L = \lambda/4$ $L/d = 13$	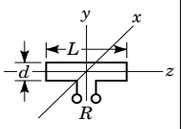	6000	5	1.64	–0.5	h	B
Folded dipole $L = \lambda/2$ $L/d = 25.5$	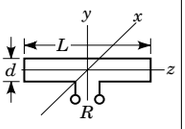	300	45	2.14	0	h	B
Biconical $L = \lambda/2$	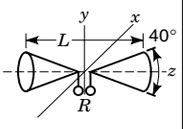	72	100	2.14	0	h	B
Biconical $L = \lambda$	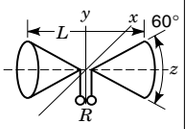	350	200	2.14	0	h	B
Turnstile $L = \lambda/2$ $L/d = 25.5$	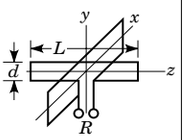	150	50	–0.86	–3	h	C
Folded dipole over reflecting sheet $\lambda L = /2$ $L/d = 25.5$ $\lambda/8$ above sheet	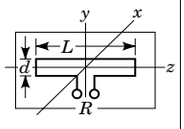	150	20	7.14	5	h	D

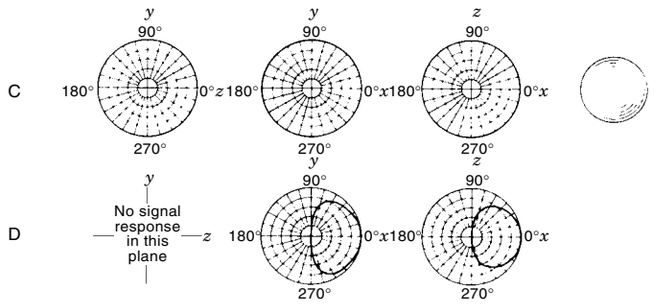

reversed. Thus, the electric-field Green's dyad for the PEC becomes

$$\vec{\mathbf{G}}_{\mathrm{PG}}(\mathbf{r},\mathbf{r}') = \vec{\mathbf{G}}_{\infty}(\mathbf{r},\mathbf{r}') + \vec{\mathbf{G}}_{\mathrm{I}}(\mathbf{r},\mathbf{r}') \tag{8a}$$

where the image term, denoted by subscript "I" is given by

$$\begin{aligned} \vec{\mathbf{G}}_{\mathrm{I}}(\mathbf{r},\mathbf{r}') &= -\vec{\mathbf{I}}_{\mathrm{R}} \cdot \vec{\mathbf{G}}_{\infty}(\mathbf{r}, \vec{\mathbf{I}}_{\mathrm{R}} \cdot \mathbf{r}') \\ \vec{\mathbf{I}}_{\mathrm{R}} &= \hat{\mathbf{x}}\hat{\mathbf{x}} + \hat{\mathbf{y}}\hat{\mathbf{y}} - \hat{\mathbf{z}}\hat{\mathbf{z}} \end{aligned} \tag{8b}$$

with a similar expression for the magnetic-field form

$$\vec{\Gamma}_{\mathrm{PG}}(\mathbf{r},\mathbf{r}') = \vec{\Gamma}_{\infty}(\mathbf{r},\mathbf{r}') + \vec{\Gamma}_{\mathrm{I}}(\mathbf{r},\mathbf{r}') \tag{8c}$$

$$\vec{\Gamma}_{\mathrm{I}}(\mathbf{r},\mathbf{r}') = -\vec{\mathbf{I}}_{\mathrm{R}} \cdot \vec{\Gamma}_{\infty}(\mathbf{r}, \vec{\mathbf{I}}_{\mathrm{R}} \cdot \mathbf{r}') \tag{8d}$$

Then the Pocklington IE is written without any additional approximation as

$$\hat{\mathbf{s}} \cdot \mathbf{E}^{\mathrm{i}}(s) = \frac{1}{4\pi j\omega\epsilon} \int_{C(\mathbf{r})} I(s')[G_{\infty}(s,s') + G_{\mathrm{I}}(s,s'^{*})]ds'$$

Table 1. *(Continued)*

Type	Configuration	Impedance: Resistive at f_r·9 $R(\Omega)$	–3-dB Bandwidth Percent	Gain: dB above Isotropic	Gain: dB above Dipole	Polarization	Pattern number
Dipole over small ground plane $L = \lambda/4$ $L/D = 53$ $l = 2\lambda$	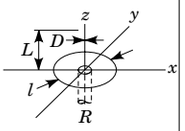	28	40	2.14	0	v	B
Folded unipole over small ground plane $L = \lambda/4$ $L/D = 53$ $l = 2$ $L/d = 13$	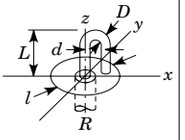	150	45	2.14	0	v	B
Coaxial dipole $L = \lambda/4$ $L/D = 40$	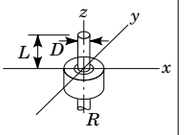	50	16	2.14	0	v	B
Biconical coaxial dipole $L = \lambda/2$ $d = \lambda/8$ $D = 3\lambda/8$	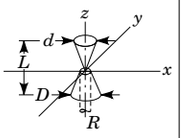	72	200	2.14	0	v	B
Disc-cone or rod disc-cone $L = \lambda/4$ $l = \lambda$	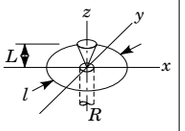	50	300	2.14	0	v	B
Biconical horn $L = 9\lambda/2$ $D = 14\lambda$	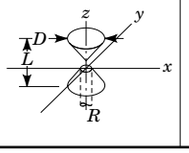	20	25	14.14	12	v	B

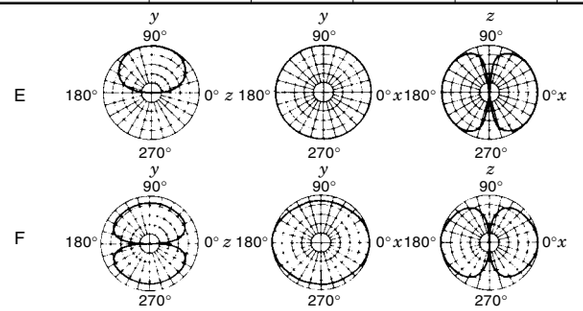

with

$$
\begin{aligned}
G_{\mathrm{I}}(s, s'^*) &= [k_\infty^2 \hat{\mathbf{s}} \cdot \hat{\mathbf{s}}'^* + (\hat{\mathbf{s}} \cdot \nabla)(\hat{\mathbf{s}}'^* \cdot \nabla)] g_{\mathrm{I}}(R^*) \\
g_{\mathrm{I}}(R^*) &= \frac{e^{-jk_\infty R^*}}{R^*} \\
R* &= |\mathbf{r} - \mathbf{r}'^*| \\
\mathbf{r}'^*(x, y, z) &= \mathbf{r}'(x, y, -z) \\
\hat{\mathbf{s}}'^* &= \frac{\nabla C(\mathbf{r}'^*)}{|\nabla C(\mathbf{r}'^*)|}
\end{aligned}
\tag{9}
$$

with the effect of the PEC ground included in the G_{I} (image) term of the modified IE and where s′* is the axial coordinate of the image current. Note that image theory is useful in numerous other ways in electromagnetics, but space precludes discussing details here.

Imperfectly Conducting Ground

Modified Image Theory or Reflection-Coefficient Approximation. When the half-space of interest is finitely conducting or

Table 1. *(Continued)*

Type	Configuration	Impedance: Resistive at f_r·9 $R(\Omega)$	–3-dB Bandwidth Percent	Gain: dB above Isotropic	Gain: dB above Dipole	Polarization	Pattern number
Slot in large ground plane $L = \lambda/2$ $l/d = 29$	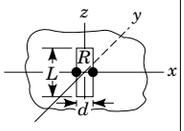	350	70	2.14	0	h	E
Vertical full-wave loop $D = \lambda/\pi$ $D/d = 36$	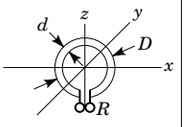	45	13	3.14	1	h	F
Helical over reflector screen, tube 6λ long coiled into 6 turns $\lambda/4$ apart	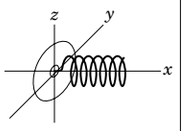	130	200	10.14	8	circ.	G
Rhombic $L = 9\lambda$ $l = 9\lambda/2$	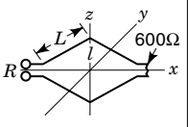	600	100	16.74	14.5	h	H
Parabolic with folded dipole feed ($\lambda/2$) $D = 5\lambda/2$	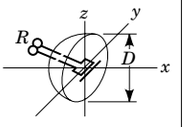	300	30	14.74	12.5	h	H
Horn, coaxial feed $L = 3\lambda$ $l = 3\lambda$	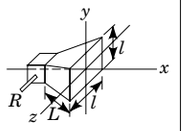	50	35	15.14	13	h	H

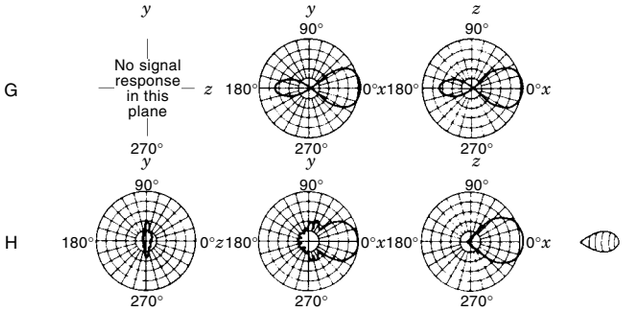

a simple dielectric, then the image-theory approach for the PEC half-space is no longer exact. Nevertheless, as a means of approximating the effect of the half-space, and thereby avoiding the considerable complexity that otherwise results from the rigorous Sommerfeld approach, a modified image theory is useful. This leads to the reflection-coefficient approximation (RCA) (1,10) and yields a new form for the Pocklington-type IE which follows from the following RCA Green's dyads

$$\vec{\mathbf{G}}_{\mathrm{IG}}(\mathbf{r},\mathbf{r}') = \vec{\mathbf{G}}_{\infty}(\mathbf{r},\mathbf{r}') + R_{\mathrm{M}}\vec{\mathbf{G}}_{\mathrm{I}}(\mathbf{r},\mathbf{r}') + (R_{\mathrm{E}} - R_{\mathrm{M}})[\vec{\mathbf{G}}_{\mathrm{I}}(\mathbf{r},\mathbf{r}')\cdot\hat{\mathbf{p}}]\hat{\mathbf{p}}$$

$$\vec{\Gamma}_{\mathrm{IG}}(\mathbf{r},\mathbf{r}') = \vec{\Gamma}_{\infty}(\mathbf{r},\mathbf{r}') + R_{\mathrm{E}}\vec{\Gamma}_{\mathrm{I}}(\mathbf{r},\mathbf{r}') + (R_{\mathrm{M}} - R_{\mathrm{E}})[\vec{\Gamma}_{\mathrm{I}}(\mathbf{r},\mathbf{r}')\cdot\hat{\mathbf{p}}]\hat{\mathbf{p}}$$

$$\hat{\mathbf{p}} = \frac{(\mathbf{r}-\mathbf{r}')\times\hat{\mathbf{z}}}{|(\mathbf{r}-\mathbf{r}')\times\mathbf{z}|} \tag{10}$$

Table 2. Different Forms of Thin-Wire-Approximation Integral Equations[a]

$$\hat{\mathbf{s}}\cdot\mathbf{E}^{\mathrm{i}}(s) = \frac{1}{4\pi j\omega\varepsilon_\infty}\left(\frac{\partial}{\partial s}\nabla\cdot + k_\infty^2\hat{\mathbf{s}}\cdot\right)\int_{C(\mathbf{r})}\hat{\mathbf{s}}'\mathrm{I}(s')g_\infty(R)ds'$$

$$\hat{\mathbf{s}}\cdot\mathbf{E}^{\mathrm{i}}(s) = \frac{1}{4\pi}\int_{C(\mathbf{r})}\left[\hat{\mathbf{s}}\cdot\hat{\mathbf{s}}'j\omega\mu_\infty I(s')g(R) - \frac{1}{j\omega\varepsilon_\infty}\frac{\partial I(s')}{\partial s'}\hat{s}\cdot\nabla g_\infty(R)\right]ds'$$

$$\hat{\mathbf{s}}\cdot\mathbf{E}^{\mathrm{i}}(s) = \frac{1}{4\pi}\int_{C(\mathbf{r})}\hat{\mathbf{s}}\cdot\hat{\mathbf{s}}'j\omega\mu_\infty I(s')g_\infty(R)ds' - \frac{1}{4\pi j\omega\varepsilon_\infty}\frac{\partial}{\partial S}\int_{C(\mathbf{r})}\frac{\partial I(s')}{\partial s'}g_\infty(R)ds'$$

Pocklington's Integral Equation

$$\hat{\mathbf{s}}\cdot\mathbf{E}^{\mathrm{i}}(s) = \frac{1}{4\pi j\omega\varepsilon_\infty}\int_{C(\mathbf{r})}I(s')G_\infty(s,s')ds', \text{ with } G_\infty(s,s') = [k_\infty^2\hat{\mathbf{s}}\cdot\hat{\mathbf{s}}' + (\hat{\mathbf{s}}\cdot\nabla)(\hat{\mathbf{s}}'\cdot\nabla)]g_\infty(R)$$

Magnetic Vector Potential Integral Equation for Arbitrarily Curved Wires

$$\int_{C(\mathbf{r})}I(s')\left[g_\infty(R)\hat{\mathbf{s}}\cdot\hat{\mathbf{s}}' + \frac{1}{2}\int_{C(\mathbf{r})}d\xi\theta(\xi-s)e^{-jk_\infty|s-\xi|}\left\{\frac{\partial}{\partial s'}g_\infty(R)(\hat{\xi}\cdot\hat{\mathbf{s}}') + \frac{\partial}{\partial\xi}[(\hat{\xi}\cdot\hat{\mathbf{s}}')g_\infty(R)]\right)\right\}ds'$$

$$= Ae^{-jk_\infty s} + Be^{jk_\infty s} + \frac{1}{2\sqrt{(\mu_\infty/\varepsilon_\infty)}}\int_{C(\mathbf{r})}\hat{\mathbf{s}}\cdot\mathbf{E}^{\mathrm{i}}(s')e^{-jk_\infty|s-s'|}ds'$$

$$\theta(u) = 1,\ u \geq 0;\ \theta(u) = 0,\ u < 0$$

Magnetic Vector Potential Integral Equation for Straight Wires (Hallen's Integral Equation)

$$\int_{C(\mathbf{r})}I(s')g_\infty(R)ds' = A^{-jk_\infty s} + B^{jk_\infty s} + \frac{1}{2\sqrt{(\mu_\infty/\varepsilon_\infty)}}\int_{C(\mathbf{r})}\hat{\mathbf{s}}\cdot\mathbf{E}^{\mathrm{i}}(s')e^{-jk_\infty|s-s'|}ds'$$

In the previous equations:

s and s' denote the axial coordinates at the observation and source points, respectively;

$\mathbf{r}$ and $\mathbf{r}'$ are the vector coordinates at the observation and source points;

$\hat{\mathbf{s}} = \dfrac{\nabla C(\mathbf{r})}{|C(\mathbf{r})|}$ and $\hat{\mathbf{s}}' = \dfrac{\nabla C(\mathbf{r}')}{|C(\mathbf{r}')|}$ are unit tangent vectors at $\mathbf{r}$ and $\mathbf{r}'$;

$C(\mathbf{r})$ is the range of integration over the wire;

$a(\mathbf{r})$ is the wire radius at $\mathbf{r}$;

$s \in C(\mathbf{r}) + a(\mathbf{r})$ so that $R \geq a(\mathbf{r})$ as required by the thin-wire approximation;

$g_\infty(R) = \dfrac{e^{-jk_\infty R}}{R}$;

$R = [a(\mathbf{r}')^2 + |\mathbf{r} - \mathbf{r}'|^2]^{1/2}$;

$k_\infty = \omega/(\mu_\infty\varepsilon_\infty)^{1/2}$ is the wave number of the infinite medium in which the wire is located; the superscript "i" denotes an incident-field quantity; and the "^" denotes a unit-length vector.

[a] After (1).

as

$$\hat{\mathbf{s}}\cdot\mathbf{E}^{\mathrm{i}}(s) = \frac{1}{4\pi j\omega\epsilon}\int_{C(\mathbf{r})}\mathrm{I}(s')[G_\infty(s,s') + R_{\mathrm{M}}G^{\mathrm{I}}(s,s'^*) + (R_{\mathrm{E}} - R_{\mathrm{M}})\sin\beta\sin\beta'\sin(\varphi-\alpha)\sin(\phi-\alpha')g_{\mathrm{I}}(R^*)]ds' \tag{11a}$$

where

$$R_{\mathrm{E}} = \frac{(\epsilon_{\mathrm{E}} - \sin^2\theta)^{1/2} - \cos\theta}{(\epsilon_{\mathrm{E}} - \sin^2\theta)^{1/2} + \cos\theta}$$

$$R_{\mathrm{M}} = \frac{\epsilon_{\mathrm{E}}\cos\theta - (\epsilon_{\mathrm{E}} - \sin^2\theta)^{1/2}}{\epsilon_{\mathrm{E}}\cos\theta + (\epsilon_{\mathrm{E}} - \sin^2\theta)^{1/2}} \tag{11b}$$

and

$$\varphi(\mathbf{r}) = \tan^{-1}\left[\frac{(y-y')}{(x-x')}\right] \tag{11c}$$

Here R_{E} and R_{M} are the Fresnel plane-wave reflection coefficients for transverse-electric (TE) and transverse-magnetic (TM) polarizations, respectively and the subscript "IG" signifies an imperfect ground. Also, $\theta(\mathbf{r},\mathbf{r}')$ is the angle with respect to a normal to the interface and a straight line in the vertical plane that joins s and s' (known as the specular reflection point from optics), and $\alpha(\mathbf{r})$ and $\beta(\mathbf{r})$ are the directional angles of the wire at $\mathbf{r}$ with respect to the x and z axes, but these explicit dependencies are omitted for clarity. Note

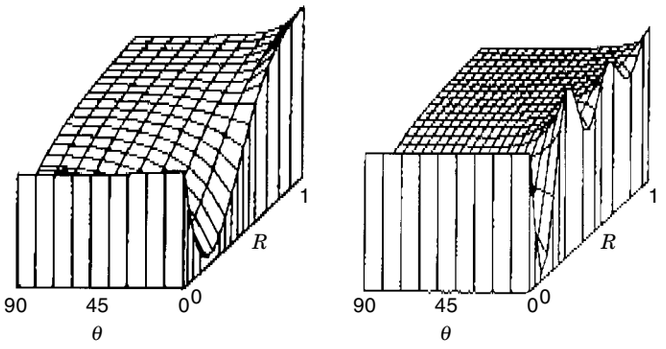

Figure 3. The real component of the radial electric field of a horizontal, delta-functional current source in free space is shown as a function of distance R and elevation angle θ near a half-space for $\epsilon_{IG}/\epsilon_\infty = 4$, $\sigma_{IG} = 0.001$ S/m, and (b) $\epsilon_{IG}/\epsilon_\infty = 16$, $\sigma_{IG} = 0$ (17). The latter exhibits the beating effect of waves in the upper and lower half-spaces with two different wavelengths which the loss in the former eliminates.

that ϵ_E is the permittivity of the lower half-space *relative* to the upper, that is,

$$\epsilon_E = \frac{\epsilon_{IG}}{\epsilon_\infty} - j\frac{\sigma_{IG}}{\omega\epsilon_\infty} = \epsilon_{Er} - j\epsilon_{Ei} \tag{12}$$

where ϵ_{IG} and σ_{IG} are the permittivity and conductivity of the lower half-space, the subscripts "r" and "i" denote real and imaginary components, and it should be understood that ϵ_∞ itself can be complex, should the above-ground medium be conducting.

The RCA provides reasonably good results for input impedance and radiation patterns, with errors of 10% or less in the former, for wires no closer than 0.1 wavelength of the interface. For situations requiring greater accuracy or involving wires closer to the interface, the Sommerfeld approach, or its equivalent, is needed.

The Sommerfeld Approach. The Sommerfeld approach expands the fields of point sources in a continuous-wave expansion along the interface, which leads to infinite-range integrals for the reflected fields that appear in place of the image terms in the RCA. Thus, one form of the Pocklington-type EFIE for the imperfect ground is written as follows (1,9,11,12):

$$\begin{aligned}\hat{\mathbf{s}}\cdot\mathbf{E}^i(s) = \frac{1}{4\pi j\omega_\infty\epsilon_\infty}\int_{C(\mathbf{r})} I(s')\Bigg(&G_\infty(s,s') + G_I(s,s'^*)\\ &+\left[k_\infty^2\cos\beta + \frac{\partial^2}{\partial s\partial z}\right][\sin\beta' g_{Hz} - \cos\beta' g_{V_z}]\\ &+\sin\beta'\left[k_\infty^2\sin\beta\cos(\alpha-\alpha') + \frac{\partial^2}{\partial s\partial t'}\right]g_{Ht}\Bigg)\,ds'\end{aligned} \tag{13}$$

where the partial derivative with respect to t' is in the direction of the horizontal projection of the wire at s'. Also

$$\begin{aligned} g_{Ht} &= 2\int_0^\infty \frac{\lambda}{\gamma_\infty+\gamma_E}J_0(\lambda\rho)e^{-\gamma_\infty(z+z')}d\lambda\\ g_{Hz} &= \frac{-\cos(\varphi-\alpha')}{k_\infty^2}\int_0^\infty \frac{\gamma_\infty-\gamma_E}{\epsilon_E\gamma_\infty+\gamma_E}J_1(\lambda\rho)e^{-\gamma_\infty(z+z')}\lambda^2 d\lambda\\ g_{Vz} &= 2\int_0^\infty \frac{\gamma_E}{\epsilon_E\gamma_\infty+\gamma_E}J_0(\lambda\rho)e^{-\gamma_\infty(z+z')}\frac{\lambda}{\gamma_\infty}d\lambda\\ \rho &= \sqrt{(x-x')^2+(y-y')^2+a^2}\\ \gamma_\infty &= \sqrt{\lambda^2-k_\infty^2}\\ \gamma_E &= \sqrt{\lambda^2-\epsilon_E k_\infty^2}\end{aligned} \tag{14}$$

where the integrals are the field expansions mentioned previously, first derived by Sommerfeld (11,13). The quantity $J_n(x)$ is a Bessel function of order n and argument x, z and z' are the source and observation heights above the interface, and the "a" in the expression for radial separation ρ imposes the minimum separation required by the thin-wire approximation. Note that these integrals are functions of only two variables ρ and $z + z'$.

The treatment thus far is limited to the "one-sided" problem, where the object being modeled is entirely contained on one side of the interface, so that the source and observation points are always in the same medium. Similar, but still more complicated expressions result when the object(s) being modeled occupy both half-spaces, that is, the "two-sided" problem. It is worth noting that the RCA has been extended to the two-sided problem (14), but the latter primarily has been approached with the Sommerfeld theory or its equivalent. Ana-

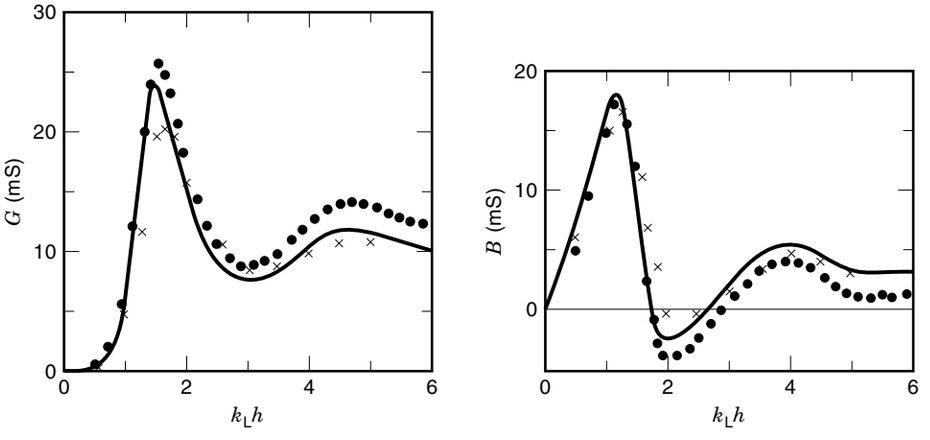

Figure 4. These three results for the input admittance of a monopole antenna of length h with air insulation $b/a = 2.5$ in water having $\epsilon_{IG}/\epsilon_\infty = 80 - j0.197$ as a function of the composite wave number demonstrate the general validity of the sheath model described above. The x's are from NEC, the solid lines are independent computations (21), and the solid circles are measurements (22).

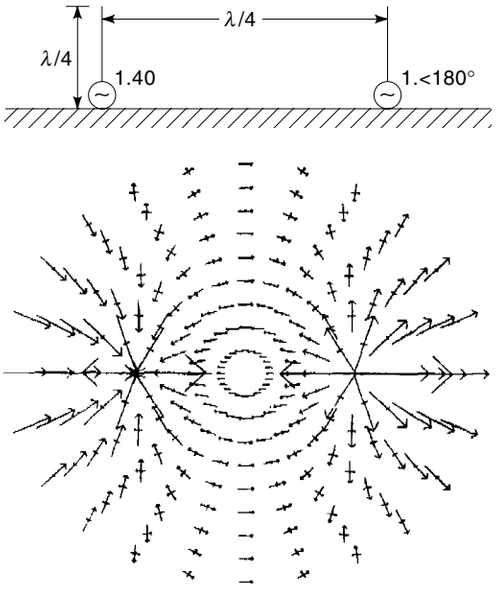

Figure 5. The two-element monopole array shown produces the ground-plane currents presented as a vector plot (24). By revealing the current-flow pattern in a perfect ground, such plots indicate the most effective ground-screen geometry. The arrows represent the semimajor and semiminor axes of the ground-current polarization ellipse, respectively.

lytical treatment of the two-sided problem is beyond the scope of this discussion. The details are found elsewhere (e.g., (12,13), but it is relevant to mention that the fields for the two-sided case are functions of the three variables ρ, z and z'.

Simplifying the Sommerfeld Treatment. The appearance of the Sommerfeld integrals as part of its kernel function adds significant further computational complexity to solving the IE in Eq. (6). There are at least three ways of reducing the computer cost of solving interfacial problems while retaining the rigor of the Sommerfeld-type approach:

1. develop more efficient ways of evaluating the Sommerfeld integrals;
2. develop an alternative, more efficient formulation in their place;
3. minimize the need for evaluating these integrals in the numerical model.

Category (1) has long been pursued, and a variety of analytical approximations have been derived for various regions of the parameter space for which Sommerfeld-integral values are needed, as have been numerous numerical approaches. Unfortunately, although some very useful results have been obtained, individual approaches generally do not cover the parameter space encountered in many practical problems, so this possibility has had only limited success. The Sommerfeld integrals are one of the wave-type, or Fourier-type expansions, developed for the interface problem, of which a summary is found in (13).

As an alternative to wave expansions that lead to Sommerfeld-type integrals, one example of category (2) is the development of complex-image theory (15). This particular approach replaces the Sommerfeld fields with a series of images in complex space that provide the interface-reflected fields. Another alternative is to generalize the problem to include the tangential electric and magnetic fields on the interface as additional unknowns in the model (16). Because the interface extends to infinity, this is impractical because the number of unknowns is commensurate with the area being modeled. However, in terms of accounting for the interaction of an object with the interface, only a limited area of the interface under the object's projection onto it measurably affects the object's currents. Thus, the number of interface unknowns is limited. Furthermore, for a particular choice of ground parameters and frequency, the interface part of the problem needs to be solved only once and then continues to be reused for whatever object is to be modeled for those specific conditions.

Approaches that fall in category (3) are of a generally different character and are described as employing a signal-processing philosophy. The basic motivation here is to compute a minimum number of Sommerfeld-integral values, or their equivalent, beyond which the field values needed in the IE

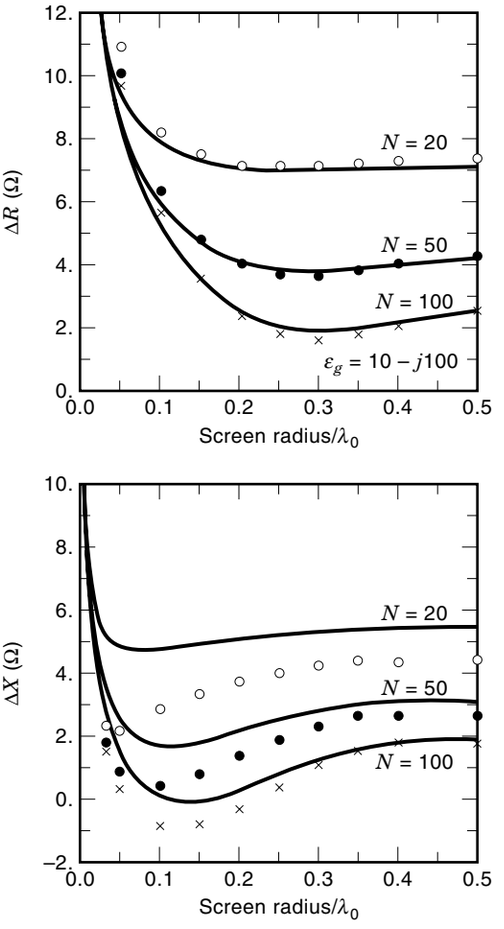

Figure 6. Input impedance of a quarter-wave monopole antenna driven against a buried ground screen with N wires subtracted from its impedance for a perfect ground with $\epsilon_E = 10 - j100$ (25). The NEC results, which represent a numerically rigorous solution of the problem are compared with approximate results from the compensation theorem (26) discussed in the next section.

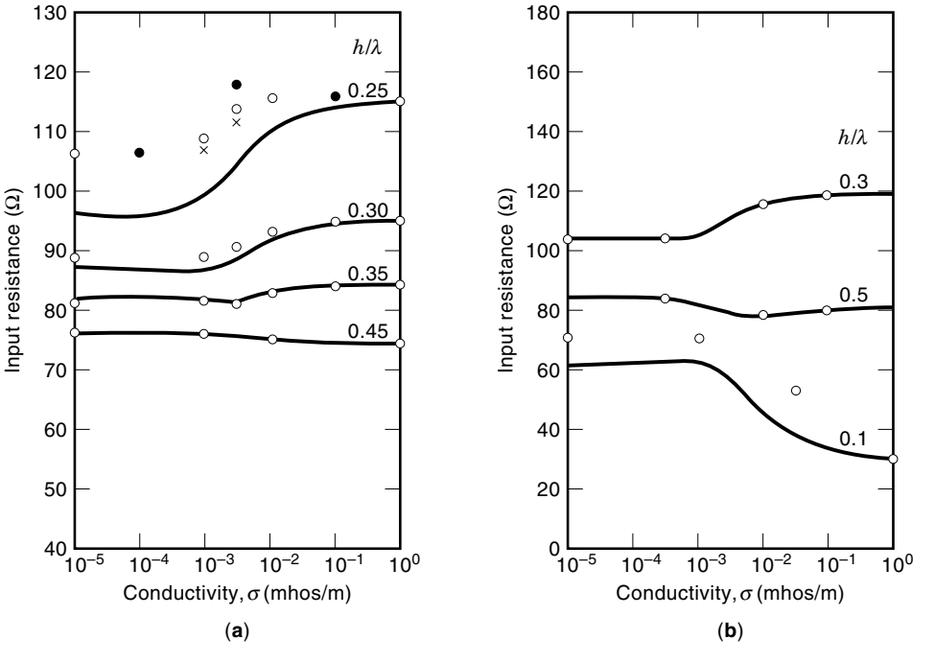

Figure 7. These plots of the input resistance of (a) a half-wave vertical dipole and (b) a half-wave horizontal dipole as a function of ground conductivity for various antenna heights compare the RCA (solid line), the Sommerfeld theory (o's), and the compensation theorem (x's) for the vertical antenna (10). The frequency is 3.0 MHz, $\epsilon_E = 10$, and the antenna radius is 5×10^{-4} wavelengths. The RCA becomes exact for PEC and so is expected to be most reliable for reasonably conductive grounds.

model are obtained from a reduced-order analytical approximation based on these values. A motivation for doing this is demonstrated in Fig. 3 (17), where the real component in the radial direction of the interfacially reflected field for a horizontal delta-function electric-current source is shown graphically as a function of the two applicable variables $R = \sqrt{[\rho^2 + (z + z')^2]}$ and $\theta = \tan^{-1}[(z + z')/\rho]$. The spatial variation of the fields is quite smooth, certainly less complex than the analytical descriptions of Eq. (14) imply. Furthermore the possibility is suggested that, if the fields are sampled over a mesh, simple interpolation might provide accurate enough values between these samples, so that no further rigorous field computations are required in numerically modeling objects near an interface, as was shown feasible (18).

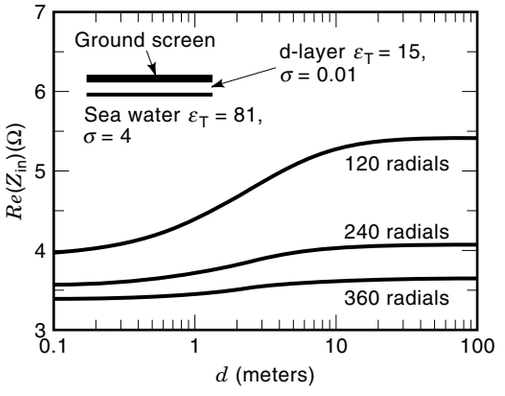

Figure 8. These results for the input resistance of the SLT as a function of depth to a salt-water half-space show that between 240 and 360 radials are needed to limit the input-resistance change to less than 10% (28). They are based on combining the RCA with Eqs. (19), (21), and (24). Also, $\epsilon_{E,1r} = 15$, $\sigma_1 = 0.01$, and $\epsilon_{E,2r} = 81$, $\sigma_1 = 4$.

However, the fields for the two-sided problem are functions of three variables and are less amenable to interpolation. But they have been similarly treated using a procedure called model-based parameter estimation (MBPE) (12). This involves using approximate, asymptotic formulas for the fields, derived from the Sommerfeld integrals as the interpolating, or fitting, functions. Matching the sum of the fitting models to rigorously computed field values provides multiplying coefficients (the parameters) for the fitting models (the parameter-estimation step). As in the simple interpolative approach, the fitting models are subsequently used in place of the Sommerfeld integrals in the numerical solution, where, for the interface problem, the computetime saving is a factor of 100–1000.

A principle that needs to be kept in mind whenever comparing alternate approaches to a given problem is that of "the conservation of difficulty." Alternative formulations that lead to integrals different from, but comparable to, the Sommerfeld integrals, may offer no computational advantage. Another principle is that of the "information content" of the phenomenon of interest. From an engineering viewpoint, only some minimum of detail is needed to acceptably represent that phenomenon, so that when there is the possibility of choosing between mathematical rigor and computational practicability, in this case between the Sommerfeld integrals and a model-based procedure, the latter offers an attractive option.

Modeling Finitely Conducting, Loaded, and Sheathed Wires

When modeling wire antennas, it is often desirable or necessary to include such effects as the distributed impedance due to a wire's finite conductivity, lumped loads when used as terminations or for matching, and dielectric sheaths used for insulation or for other purposes. The original integral equation is simply modified by including a voltage-drop term, where

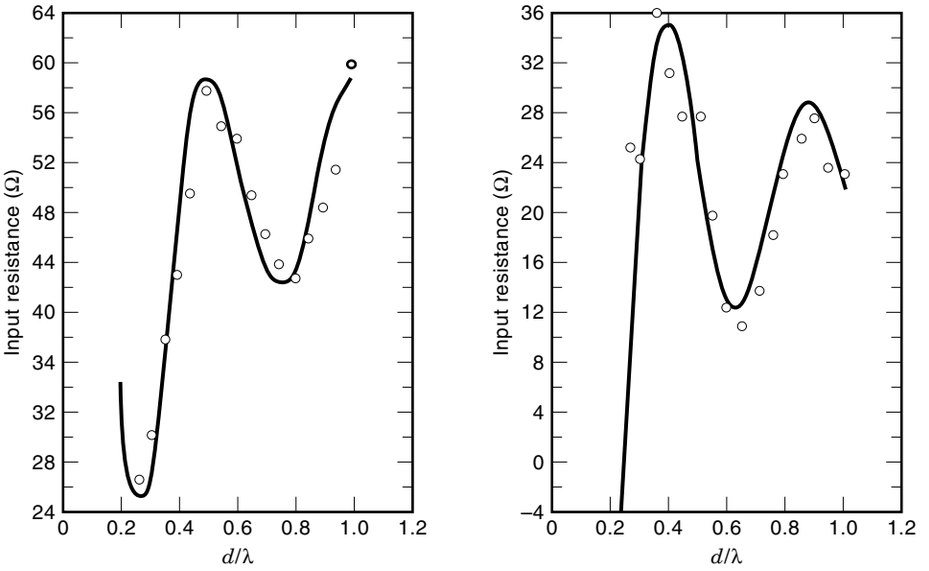

Figure 9. A hybrid of an integral equation and GTD model is used here to obtain the input impedance of a monopole antenna at the center of an octagonal plate (29). Agreement between the experimental results (open circles) and the computations (solid line) is within 10%.

$\mathbf{E}^{\mathrm{S}}(s)$ represents the field scattered from the wire by the incident field, as follows (1,2):

$$\hat{\mathbf{s}} \cdot [\mathbf{E}^{\mathrm{i}}(s) + \mathbf{E}^{s}(s)] = \hat{\mathbf{s}} \cdot \mathbf{E}^{\mathrm{i}}(s) - \frac{1}{4\pi j\omega_{\infty}} \int_{C(\mathbf{r})} I(s')G_{\infty}(s, s')ds' = Z_{\mathrm{L}}(s, s')I(s') \tag{15}$$

where $Z_{\mathrm{L}}(s, s')$ is the load value affecting the field at s because of a current at s', to allow for mutual and self-loading and whose specific value is determined as described later. For self-loading, where $Z_{\mathrm{L}}(s, s') = Z_{\mathrm{L}}(s)\delta(s - s')$, the effect of loading is simply to modify the system matrix (see below) along its diagonal, whereas mutual loading more generally affects any of the system-matrix coefficients. Mathematically, the effect of a load is the same as that of the incident-field term, except it is of opposite sign (unless it is an active load); the former represents a voltage "rise" along the wire and the latter a voltage drop.

Distributed Loading Due to Finite Conductivity. For a wire of radius a_i, conductivity σ_i, permeability μ_i, and length Δ_i, the impedance per segment i is approximately given by (2,19)

$$Z_{\mathrm{L}}(s_i) = \frac{j\Delta_i}{a_i}\sqrt{\frac{\omega\mu_i}{2\pi\sigma_i}}\left(\frac{\mathrm{Ber}(q_i) + j\mathrm{Bei}(q_i)}{\mathrm{Ber}'(q_i) + j\mathrm{Bei}'(q_i)}\right) \tag{16}$$

where

$$q_i = \sqrt{\omega\mu_i\sigma_i}a_i$$

and Ber and Bei are Kelvin functions.

Lumped-Impedance Loading. A lumped impedance is generally described as a complex quantity given by

$$Z_{\mathrm{L}}(s_i) = R_i + j\left(\omega L_i - \frac{1}{\omega C_i}\right) \tag{17}$$

for a series R, L, C load located at observation point s_i. Other combinations are readily introduced for more general situations, with the requirement that their effect is truly local and that the load is itself nonradiating except for the current flowing through it at its connection point s_i (2).

Loading Due to a Sheath. The effect of a sheathed wire is handled by including an equivalent electric current $\mathbf{J}_{\mathrm{s}}$ radiating in an infinite medium as given by (2,20)

$$\mathbf{J}_{\mathrm{s}}(\rho, s, \varphi) = j\omega\epsilon_{\infty}(\epsilon_{\mathrm{s}} - 1)[\mathbf{E}^{s}(\rho, s, \varphi) + \mathbf{E}^{i}(\rho, s, \varphi)] \tag{18a}$$

where ϵ_{s} is the permittivity of the sheath relative to the infinite medium where the wire is located. So as not to destroy the one-dimensional nature of the wire integral equation, the sheath is assumed to be electrically thin, and the total sheath field is assumed to be dominated by its radial component, which is due to the wire charge, so that

$$\mathbf{E}^{\mathrm{s}}(s) \approx \frac{\mathrm{jI}'(s)}{2\pi\omega\epsilon_{\infty}\epsilon_{\mathrm{s}}\rho}\hat{\rho} \tag{18b}$$

where $I'(s)$ is the spatial derivative of the current at s. Because the incident electric field in the radial direction can be neglected relative to that due to $I'(s)$, the equivalent sheath current becomes

$$\mathbf{J}_{\mathrm{s}}(\rho, s, \varphi) \approx \frac{-(\epsilon_{\mathrm{s}} - 1)}{2\pi\epsilon_{\mathrm{s}}\rho}I'(s)\hat{\rho} \tag{18c}$$

for $a(s) \le \rho \le b(s)$, where b is the sheath radius and a is the wire radius. As shown elsewhere (2), with some additional approximations, the sheath is predominantly a "self-term" effect, whose axial field is given by

$$\hat{\mathbf{s}}_{\mathrm{i}} \cdot \mathbf{E}^{\mathrm{s}}_{\mathrm{s}}(s_i) \approx \frac{-jk_{\mathrm{s}}^2(\epsilon_{\mathrm{s}} - 1)}{2\pi\omega\epsilon_{\infty}\epsilon_{\mathrm{s}}}C_i Ln\left[\frac{b(s_i)}{a(s_i)}\right] \tag{18d}$$

where k_{s} is the sheath wave number, to be included in the thin-wire integral equation. An example of modeling the sheath effect is shown in Fig. 4.

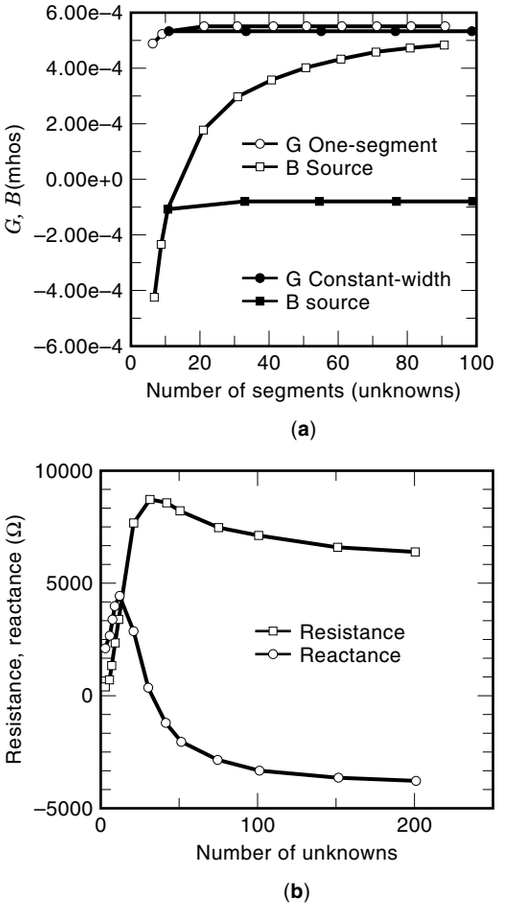

Figure 10. The input impedance (b) and admittance (a) are shown for an $L = 2\lambda$, center-fed dipole antenna as a function of the number of unknowns, where only the center segment is excited. The results imply that the impedance is not well-converged whereas the admittance behavior suggests otherwise. When multiple segments are excited to keep the physical width of the source region a constant value of $L/11$, the additional results of (b) are obtained. It's clear that physical and numerical effects influence the apparent convergence rate of the numerical solution.

Modeling Ground Screens

When used via MBPE as outlined previously, the Sommerfeld treatment can be regarded as a numerically rigorous approach for modeling antenna-ground-screen combinations for not too great an increase in computational cost compared with modeling the same configuration in an infinite medium. However, the size in wavelengths of complex screen geometries can be so large itself to make a more efficient model desirable so long as it offers acceptable accuracy. Two approaches to ground-screen modeling are outlined here, one using a surface-impedance approximation together with the RCA and the other a technique known as the compensation theorem.

Surface-Impedance Approximation for Ground Screens. The surface-impedance approximation (SIA) represents the wires in an actual ground screen by approximating the change they cause in the reflecting properties of the imperfect ground. Thus the reflection coefficients in the RCA are determined by the angle of incidence at the specular reflection point and also by the effective value of the surface impedance there. To begin with, note that the surface impedance of the imperfect ground itself is given by

$$Z_{\text{surf}} = \sqrt{\mu_{\text{IG}}/\epsilon_{\text{IG}}} = \eta_\infty/\sqrt{\epsilon_{\text{E}}} \tag{19a}$$

where η_∞ is the wave impedance of the upper medium. Then the SIA is expressed as

$$\mathbf{E}_{x,\text{IG}} = -Z_{\text{surf}}\mathbf{H}_{y,\text{IG}}$$

and (19b)

$$\mathbf{E}_{y,\text{IG}} = Z_{\text{surf}}\mathbf{H}_{x,\text{IG}}$$

which is valid when $|\sin^2\theta/\epsilon_{\text{E}}| \ll 1$ is satisfied.

For a wire ground screen located at the interface and in good electrical contact with the lower half-space so that it is considered electrically in parallel with the ground, the modified surface impedance for the imperfect ground is given by (23)

$$Z'_{\text{surf}} = \frac{Z_{\text{surf}}Z_{\text{screen}}}{Z_{\text{surf}} + Z_{\text{screen}}} \tag{20}$$

where Z_{screen} is the screen impedance. The screen impedance for a radial screen at a distance ρ from its center and comprised of N wires of radius a is given by

$$Z_{\text{screen,rad}} = \frac{j\mu_\infty\omega\rho}{N} Ln\left(\frac{\rho}{Na}\right) \tag{21a}$$

and a corresponding formula for a parallel grid of wires whose center spacing is d is

$$Z_{\text{screen,par}} = \frac{j\mu_\infty\omega d}{2\pi} Ln\left(\frac{d}{2\pi a}\right) \tag{21b}$$

thus providing a means of obtaining a value for the relative permittivity of the ground using Eq. (20) and thereby the Fresnel reflection coefficient for the RCA. It is worth observing that the latter becomes zero when $d = 2\pi a$, that is, when the area of the screen wires equals that of the surface they cover, as previously discussed in connection with using wire meshes as approximations to continuous surfaces.

Unless made of a square mesh, the impedance of a ground screen varies with direction in the x–y plane, that is, is anisotropic. Thus, implementing the RCA requires a further decomposition of the interactive field between source and observation segments that takes this anisotropy into account. The electric field is first decomposed into components along the principal directions of the screen wires relative to the specular point. For example, in the case of the parallel screen of Eq. (21b), the component parallel to the screen wires reflects from a medium whose effective permittivity, then is, given by

$$\begin{aligned}\sqrt{\epsilon'_{\text{E}}} = \eta_\infty/Z'_{\text{surf}} &= \eta_\infty\left(\frac{Z_{\text{surf}} + Z_{\text{screen}}}{Z_{\text{surf}}Z_{\text{screen}}}\right) \\ &= \eta_\infty\left[\frac{\eta_\infty + \sqrt{\epsilon_{\text{E}}}\dfrac{j\mu_\infty\omega d}{2\pi} Ln\left(\dfrac{d}{2\pi a}\right)}{\eta_\infty\dfrac{j\mu_\infty\omega d}{2\pi} Ln\left(\dfrac{d}{2\pi a}\right)}\right]\end{aligned} \tag{22}$$

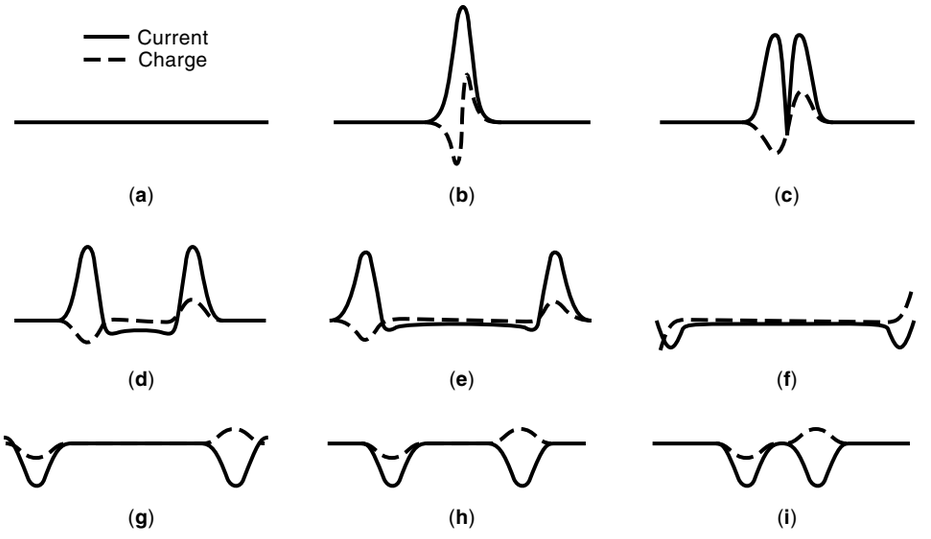

Figure 11. Current and charge "snapshots" at several time steps for a Guassian-pulse-excited dipole exhibit a variety of important physics (31). Two outward-propagating same-sign current pulses, and opposite-sign charge pulses originate from the source. A slight diminution of the pulse amplitudes occurs because of radiation damping, and a further diminution occurs upon end reflection, a strong source of radiation. Plots like these are remarkably insightful in revealing why antennas behave the way they do.

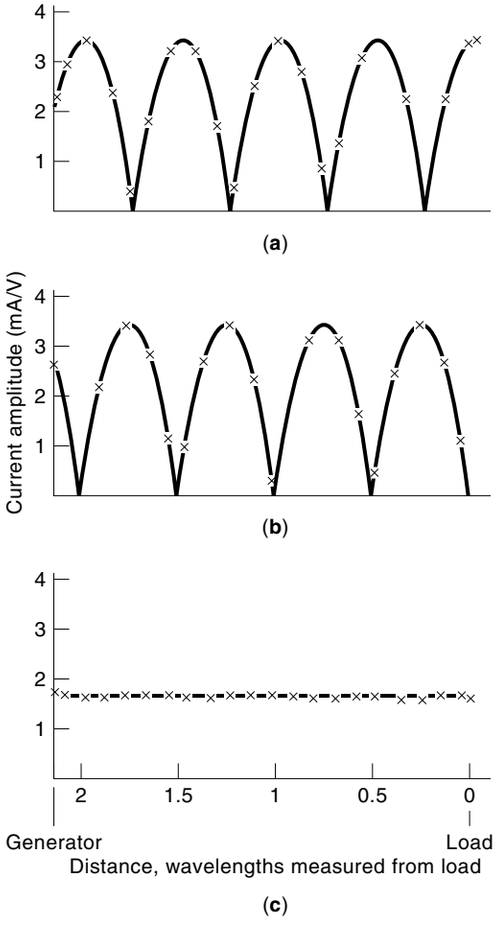

Figure 12. Comparison of current on a two-wire transmission line obtained from the analytical solution (solid line) and from a thin-wire integral equation (x's) for an (a) open circuit, (b) short circuit, and (c) matched load (16). Although these results do not check the radiative-predictive properties of the numerical model, they do provide some assurance that the model can handle a non-radiating problem.

whereas the orthogonal component reflects from a medium of permittivity ϵ_E. Then each of these two fields is further decomposed into TE and TM components relative to the specular plane and for which the appropriate Fresnel plane-wave reflection coefficients are computed and applied to determine the total reflected field at the observation segment.

Application to Ground-Screen Design. A ground screen is used to improve antenna performance by simulating a perfect-image plane to the degree necessary for the particular problem requirements. Any overdesign of the ground screen which provides an improvement greater than that sought is regarded as an inefficient allocation of resources. A reliable and credible method for optimizing the ground-screen design has a significant impact on the installation and operating costs of large antenna systems.

Observe that simulating a perfect-image plane with the ground screen implies that the ground screen should simulate current-conduction paths similar to those that occur when the same antenna is located over a perfect ground. If the current flow in the perfect ground is confined along particular paths, for example, then a ground screen with relatively few wires is still highly efficient if the wires, which it has, follow the same paths. Hence, a radial-wire ground screen is very effective for monopole antennas located at its center, because the monopole produces entirely radial ground currents.

A method for determining an optimum ground-screen geometry for a given antenna system can be developed based on the RCA as described below. The antenna is first modeled using a PEC ground from which the current-flow pattern in the ground plane under the antenna is obtained. Next, the initial ground-screen design is achieved with a wire geometry that replicates the current-flow pattern in the PEC ground with a wire spacing inversely proportional to the surface-current density and chosen to produce a specified power loss per unit area. To reduce the screen complexity, some relaxation in the actual screen geometry from the ideal pattern should be anticipated, possibly limiting the final form to a combination of rectangular cells and radial lines. To illustrate this approach, the perfect ground currents for a simple antenna are presented in Fig. 5.

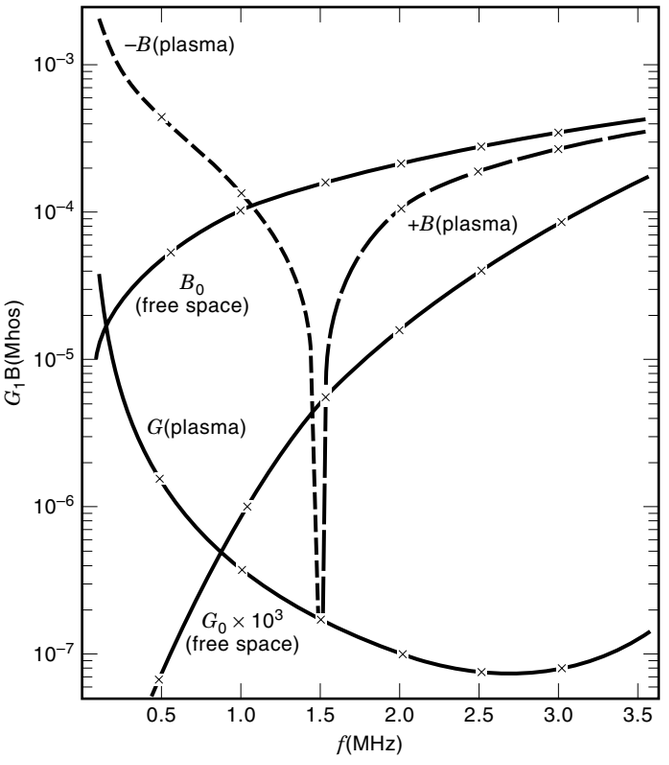

Figure 13. Comparison of results from the analytical formula of (35) (lines) with a thin-wire IE for a short antenna in free space and in a lossy plasma (x's) provides mutual validation for both approaches (16). This is an important extension of the IE model because handling lossy media is necessary for modeling antennas buried in the ground.

Using Sommerfeld Theory to Model Ground Screens. Although intended primarily for modeling antennas near an interface, the Sommerfeld approach, as included in the NEC, is also efficient enough to include the ground-screen wires for some of the simpler designs. An example demonstrating this application is presented in Fig. 6 (25).

Using the Compensation Theorem. An alternative approach to including the effects of ground screens and the interface itself on antenna impedance is a technique widely used before computer solutions became practical, but still effective for some applications. This is the compensation theorem (26), whereby the input impedance in an antenna located near an interface is estimated from a reference solution for a PEC half-space, as

$$Z_{\text{in,IG}} = Z_{\text{in,PG}} + \frac{1}{I_{\text{in,PG}} I^*_{\text{in,PG}}} \int_{\text{A}} \mathbf{H}_{\text{PG}}(x,y) \cdot \hat{\mathbf{z}} \times \mathbf{E}_{\text{IG}}(x,y) dx dy \tag{23a}$$

where the subscripts PG and IG, as before, refer to quantities associated with a perfect ground and imperfect ground, respectively. Upon using the surface-impedance approximation of Eq. (19b) and further assuming that

$$\mathbf{H}_{x,\text{IG}} = \mathbf{H}_{x,\text{PG}} \text{ and } \mathbf{H}_{y,\text{IG}} = \mathbf{H}_{y,\text{PG}} \tag{23b}$$

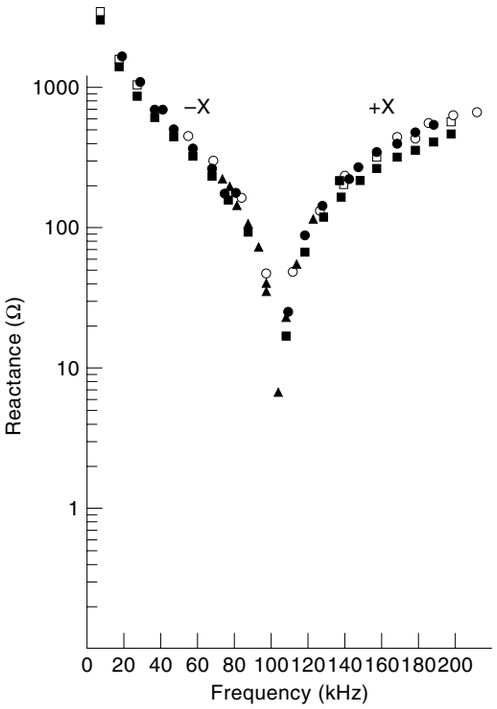

Figure 14. A comparison of the input impedance of a Vee-dipole antenna obtained from several different wire IE models shows that they agree to an order of ±30% except for the resistance at lower frequencies when decreases as f^2 (16).

then the IG input impedance is obtained entirely in terms of the PG result. Some results comparing the compensation theorem, the RCA, and the Sommerfeld integrals for modeling half-wave vertical and horizontal dipoles are included in Fig. 7.

Modeling Layered Grounds

The SIA can also be used as an approximation for modeling layered grounds in place of the even more complicated Sommerfeld approach. A particular example of interest is that of

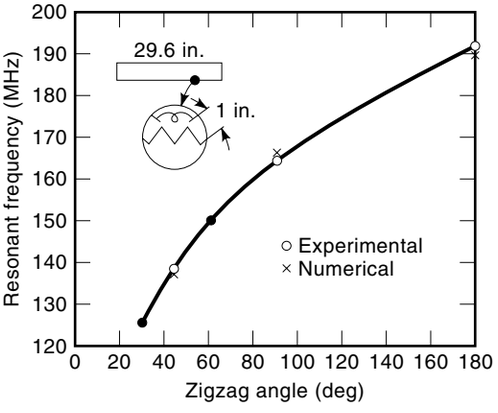

Figure 15. The computed and measured resonance frequency of a 29.6-in zigzag dipole comprised of 1-in pieces of wire agree to within 2–3%, demonstrating the capability of the wire IE model to handle a slow-wave structure (16).

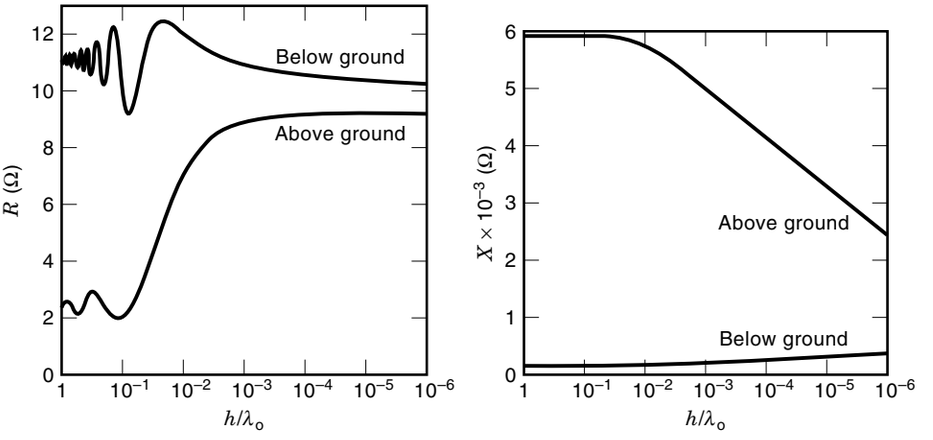

Figure 16. Although the thin-wire approximation limits how close a wire can approach an interface, by using a small radius of 10^{-8} wavelengths in free space, the 0.1 wavelength wire can be brought much closer than its length to an interface of relative permittivity = 16 (17). The above-ground results approach an asymptotic value, whereas those below ground continue to change. The smoothness of the behavior shown here does not prove the validity of the model, but does show that the model, based on the MBPE form of the Sommerfeld approach, exhibits appropriate behavior.

antennas located near a body of water, fresh or saline, where tidal effects vary the ground-water depth beneath the antenna with time of day. When an antenna's input impedance must be limited between narrowly defined values to maintain matched conditions with the generator, it is necessary to determine the ground-screen parameters that make this possible. It is straightforward to obtain an approximate value for the effective surface impedance (27) for a layer of thickness h over a lower half-space from the expression

$$Z'_{\text{surf}} = Z_{\text{surf}} \frac{\sqrt{\epsilon_{\text{E},1}} + j\sqrt{\epsilon_{\text{E},2}} \tan[k_\infty h \sqrt{\epsilon_{\text{E},1}}]}{\sqrt{\epsilon_{\text{E},2}} + j\sqrt{\epsilon_{\text{E},1}} \tan[k_\infty h \sqrt{\epsilon_{\text{E},1}}]} \tag{24}$$

where the subscript "1" applies to the upper layer and "2" to the lower half-space and, as before, ϵ_x is the permittivity relative to that of the uppermedium ϵ_∞. Including this SIA with a ground-screen approximation and the RCA provides a means for modeling the combined effect of a layered ground and ground screen. Use of the SIA for the U.S. Coast Guard Sectionalized Loran Transmitting (SLT) antenna (28) (see Fig. 22 for a computer plot of the SLT geometry) antenna is illustrated in Fig. 8.

Hybrid Models

Unfortunately, a numerical model based on a single formulation is not equally applicable to all problems. Even though a wire code models surfaces approximated as grids, there are more efficient and accurate ways to handle PEC objects. It is equally true that not all parts of a given problem are suitable for modeling with a single formulation. Wires attached to solid PEC objects or located near inhomogeneous dielectric bodies are simple examples. For this reason, it is desirable to combine two (or more) approaches to develop what is called a "hybrid" model to handle such problems.

Considering that there are four kinds of numerical models presently used in electromagnetics (EM), based on integral equations, differential equations, modal expansions and the geometrical theory of diffraction (GTD), formulated in either the frequency domain or time domain, hybrid models have been developed using various combinations of these (see (29,30) for two examples). An especially useful hybrid model involving wires is one that combines a wire IE with the GTD, an example of which is shown in Fig. 9. The benefit of this kind of hybrid model is that only the unknowns for the cur-

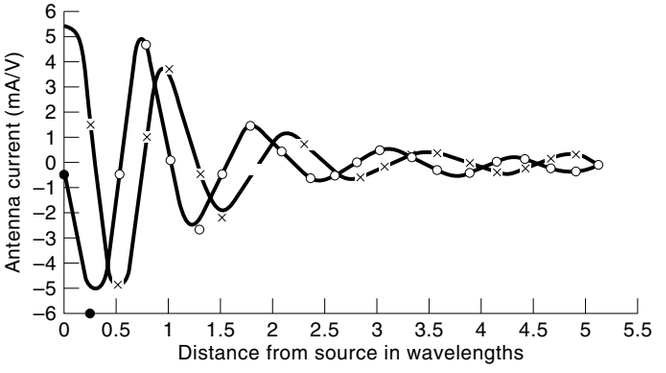

Figure 17. The real (x) and imaginary (o) components of the current on a conical spiral antenna obtained from a Pocklington IE compared with a Hallen IE (solid and dashed lines) (36) show agreement to within about 10% (16). The difficulty of generalizing the Hallen IE to arbitrary geometries restricts its application.

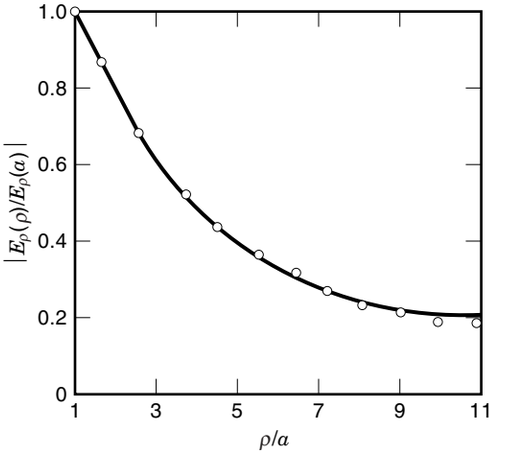

Figure 18. The normalized, near, radial electric field of a circular loop antenna obtained from the electric-field IE (o's) (16) agrees within a few percent, on a normalized basis, with analytical results (solid line) (37).

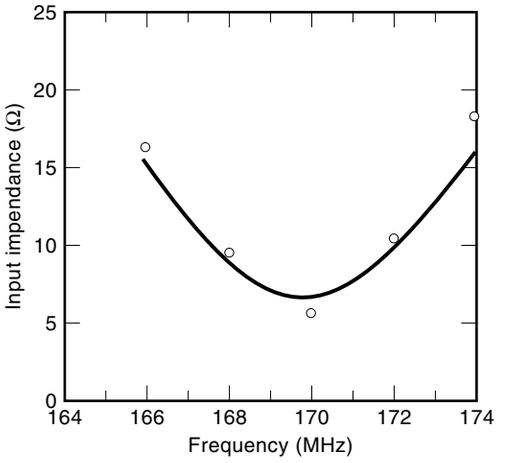

Figure 19. This comparison between the electric-field IE (o) and measured data (solid line) of the frequency response of a circular loop continuously loaded with capacitors demonstrates the possibility of modeling a distributed capacitive load (16).

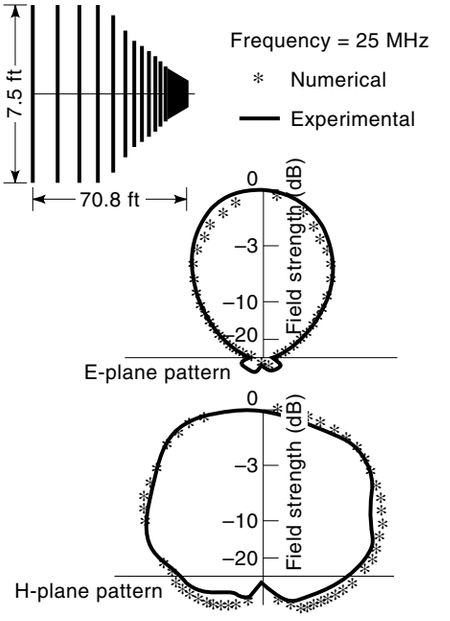

Figure 20. Lumped loading is employed here to foreshorten the four longest elements in a 19-element log-periodic antenna, with agreement to ±1 dB relative to the pattern maximum obtained between experimental measurements (lines) and numerical results (solid circles) (16).

rents on the wire need to solved for, because the currents on the plate, against which the monopole is driven, are accounted for via GTD diffraction coefficients.

Modeling in the Time Domain

Equations analogous to those in the frequency domain can be derived for many situations directly in the time domain. For a wire in free space, an IE comparable to the Pocklington IE can be developed as follows (31):

$$\hat{\mathbf{s}} \cdot \mathbf{E}^{\mathrm{i}}(s,t) = \frac{\mu_\infty}{4\pi} \int_{C(\mathbf{r})} \left\{ \frac{\hat{\mathbf{s}} \cdot \hat{\mathbf{s}}'}{R} \frac{\partial I(s',t')}{\partial t'} + \left[\frac{c_\infty \mathbf{s} \cdot \mathbf{R}}{R^2} \right] \left[\frac{\partial I(s',t')}{\partial s'} - \frac{c_\infty}{R} Q(s',t') \right] \right\} ds' \quad (25)$$

$$Q(s',t') = -\int_{-\infty}^{t'} \frac{\partial I(s',t')}{\partial s'} dt'$$

where $Q(s,t)$ is the charge density at space location s and time t and the "retarded time" $t' = R/c_\infty$, where $c_\infty$is the speed of light in the medium. A time-domain IE like that in Eq. (25) is readily solved by "time stepping" whereby the solution is developed as a function of space and time, as described later.

NUMERICAL IMPLEMENTATION VIA THE MOMENT METHOD

The Frequency Domain

A generic form of the frequency-domain IEs thus far considered can be written as (1,32)

$$L(s,s')f(s') = g(s) \quad (26a)$$

where $L(s, s')$ is the integral operator, $f(s')$ is the unknown current, and $g(s)$ is the known source or forcing function, which, for our application, is sampled values of a specified tangential electric field. The method of moments (MOM) is an intuitively logical way of solving this operator equation, whereby the unknown is expressed (or sampled) in terms of a

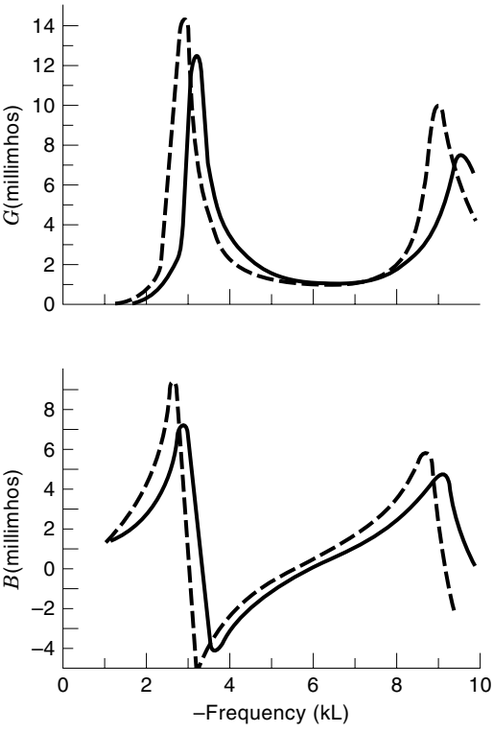

Figure 21. These plots compare the input admittance of a dipole antenna driven by a tangential electric field (dashed line) compared with one attached to a two-wire transmission line and excited at the far end (solid line) (16). The upward frequency shift caused by the transmission line is evidently caused by the capacitive-loading effect of the antenna–transmission–line junction.

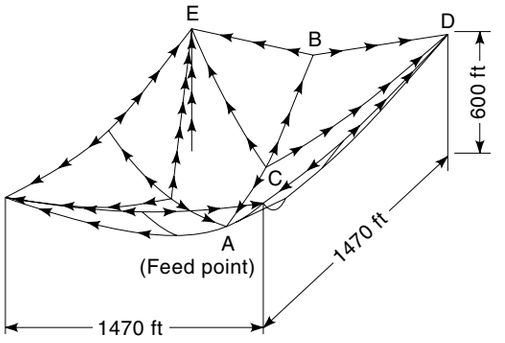

Figure 22. The computer model of the SLT antenna, containing a total of 237 wire segments demarcated by the arrows (28). At the time this work was done, a 237-segment model was state-of-the-art, but now this problem is considered small for desk-top computers.

set of basis or expansion functions $f_i(s')$ and unknown coefficients a_i:

$$f(s') = \sum_{i=1}^{N_s} a_i f_i(s') \tag{27a}$$

so that the operator equation is then written

$$L(s,s')\sum_{i=1}^{N_s} a_i f_i(s') = \sum_{i=1}^{N_s} a_i L(s,s') f_i(s') = g(s) \tag{26b}$$

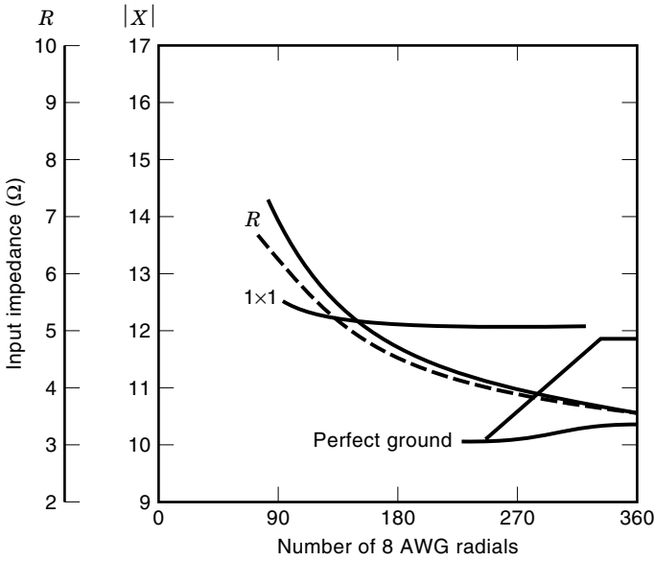

Figure 23. The influence of the number of wires in a radial-wire ground screen on the input impedance of the SLT antenna as modeled using the RCA and ground-screen approximation shows that the reactance is much less affected by a changing ground conductivity than is the resistance (16). For the dashed curves, $\epsilon_E = 15$ and $\sigma_{IG} = 10^{-2}$ S and for the solid curves $\epsilon_E = 15$ and $\sigma_{IG} = 10^{-3}$ S.

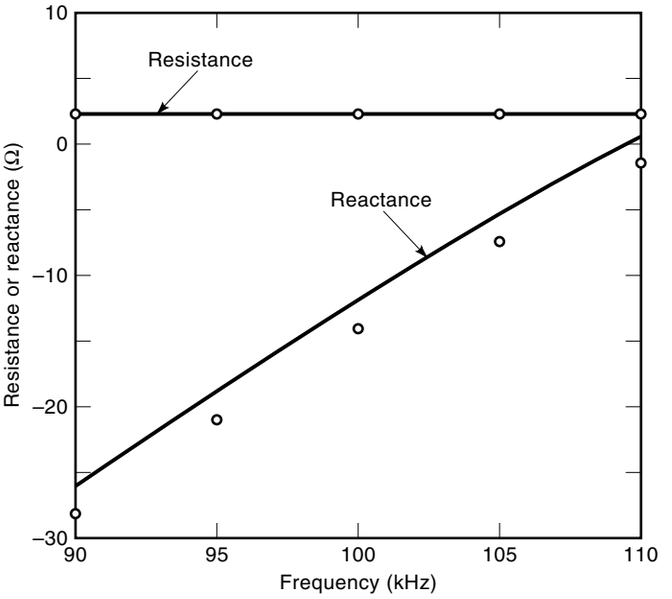

Figure 24. The modeled (o's) SLT resistance results compare within a few percent of the scale-model measurements (solid lines) while the reactance values are shifted by about 2% in frequency (16) for 120 radials in the ground screen and $\epsilon_E = 15$ and $\sigma_{IG} = 2 \times 10^{-2}$ S. Such reactance shifts are fairly common in numerical modeling, and can have a number of causes (34). Of course, besides limitations in the numerical model, incomplete knowledge of the experimental conditions can also be a source of such differences.

where N_s is the number of spatial unknowns. Then upon sampling the operator Eq. (26b) with a set of testing or weight functions

$$\{w_j(s)\},\ m = 1, \ldots, M \tag{27b}$$

$$\sum_{i=1}^{N_s} a_i \langle w_j(s), L(s,s' f_i(s')\rangle = \langle w_j(s), g(s)\rangle, m = 1, \ldots, M \tag{27c}$$

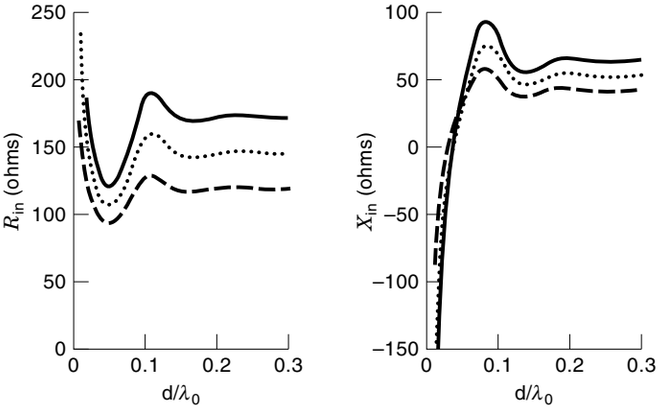

Figure 25. A numerical model like NEC makes it possible to evaluate the influence of parameters such as the length of a ground stake against which a monopole antenna is driven, as illustrated here (24), computed using the rigorous Sommerfeld approach for a wire radius of 2.5×10^{-6} (solid line), 2.5×10^{-5} (dotted line), and 2.5×10^{-4} (dashed line), respectively, for a ground of $\epsilon_E = 16 - j16$. Results like this make it feasible to determine what kind of ground stake is needed to stabilize the input impedance.

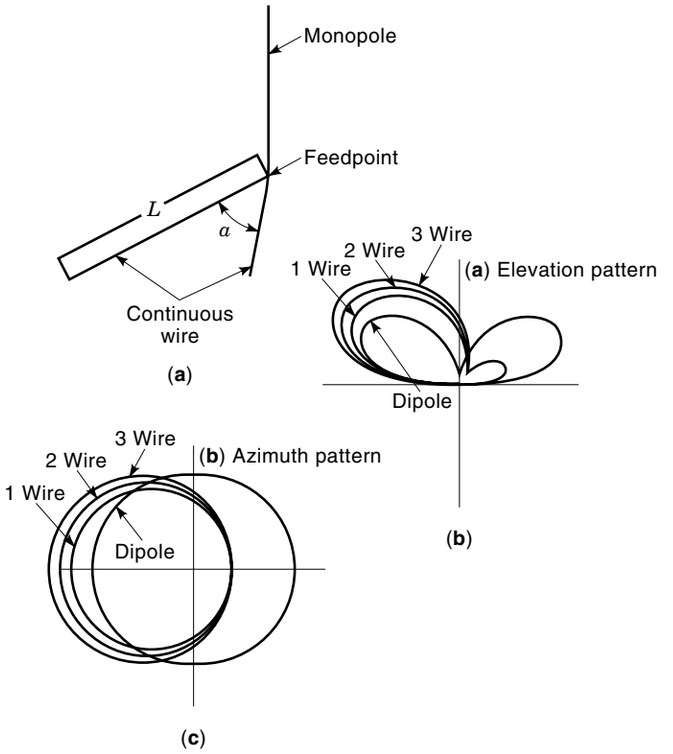

Figure 26. Sparse ground screens like that shown here (a) cannot be modeled using the simple ground-screen formulas, but can be handled using the interpolated Sommerfeld approach (38), to obtain the elevation (b) and azimuth (c) patterns, with the number of ground wires as a parameter. The frequency is 10 MHz and the ground has $\epsilon_E = 4$ and $\sigma_{IG} = 10^{-3}$ S.

where the $\langle\ \rangle$ signifies what is called an "inner product" (the inner product of two functions $p(\mathbf{r})$ and $q(\mathbf{r})$ over a surface S defined as $\int_s p(\mathbf{r})q(\mathbf{r})d^2s$).

Now the original operator equation is written in a discretized, sampled approximation as

$$\sum_{i=1}^{N_s} Z_{ji}a_i = b_j, j = 1, \ldots, M \tag{28a}$$

where

$$Z_{ji} = \langle w_j(s), L(s,s')f_i(s')\rangle$$

and (28b)

$$b_j = \langle w_j(s), g(s)\rangle$$

Finally, the coefficients that quantify the numerical solution for the current distribution are obtained as

$$a_i = \sum_{j=1}^{M} Y_{ij}b_j, i = 1, \ldots, N_s \tag{29}$$

where Z_{ij} is known as the impedance matrix and Y_{ij} is the admittance matrix, its inverse. Equations (28a) and (29) are written more compactly in symbolic form as

$$\vec{\vec{\mathbf{Z}}} \cdot \mathbf{A} = \mathbf{B} \Rightarrow \mathbf{A} = \vec{\vec{\mathbf{Y}}} \cdot \mathbf{B}$$

The admittance matrix is a numerical representation of the complete EM properties of the object being modeled, within the approximations made in its computation, and as such it has some interesting properties. First, it provides a solution for arbitrary excitation. Second, it can be stored for subsequent reuse. Perhaps most interesting, in a very real sense, it possesses the properties of a hologram, as seen by writing the field radiated by the object as

$$E_r = \sum_{i=1}^{N_s} E_i^o \sum_{j=1}^{N_s} Y_{ij}E_j^i \tag{30a}$$

where the first sum yields a solution for the current distribution and the second sums the field at a specified observation point caused by that current. Also

$$E_i^o = \hat{\mathbf{s}}_i \cdot \mathbf{E}^o(s_i) \text{ and } E_j^i = \hat{\mathbf{s}}_j \cdot \mathbf{E}^i(s_j) \tag{30b}$$

where the exciting field $\mathbf{E}^i$ and the "observation" field $\mathbf{E}^o$ are tangential projections onto the object of an arbitrary incident field and the field from a point source located at the observation point.

Much work has been done to identify the "best" expansion and testing functions. A variety of combinations are described by Poggio and Miller (1). Those in NEC use what is called "sub-sectional collocation," wherein the wire is divided into N_s "segments" with

$$f_i(s') = A_i + B_i \sin[k(s' - s_i)] + C_i\{\cos[k(s' - s_i)] - 1\}, \quad s_i - \Delta_i/2 \le s' \le s_i + \Delta_i/2, i = 1, \ldots, N_s \tag{31a}$$

and

$$w_j(s) = \delta(s - s_j), j = 1, \ldots, N_s \tag{31b}$$

where Δ_i is the length of segment i and $\delta(s - s_j)$ is a delta-function, thus producing point sampling of the tangential electric field. Of the $3N_s$ unknowns in Eq. (31), $2N_s$ are eliminated by enforcing current and current-slope (charge) conti-

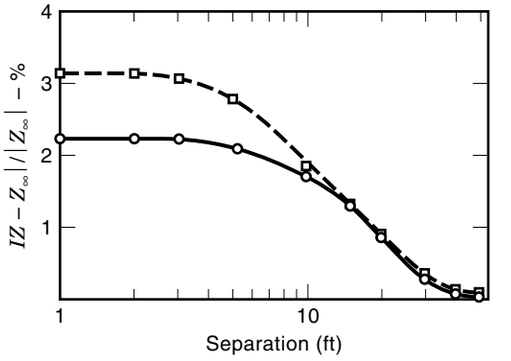

Figure 27. Comparison of the TCA (dashed line) with the Sommerfeld theory (solid line) demonstrates the former's potential applicability to subsurface probing (14) for a ground of $\epsilon_E = 9$ and $\sigma_{IG} = 10^{-3}$ S and with both wires 0.5 wavelengths long and for a frequency of 10 MHz. The goal here is to detect a buried object from its effect on the impedance of an above-ground probing antenna whose effect is plotted as a normalized difference between its value with and without the object.

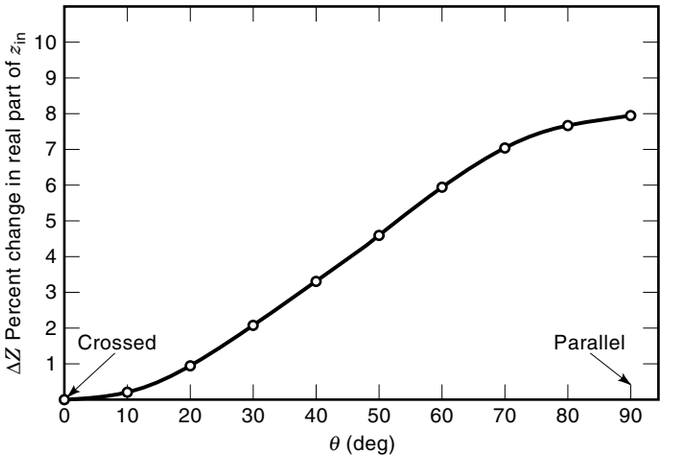

Figure 28. Here the TCA is used to determine the variation in the input impedance of an above-ground, horizontal antenna (L = 0.457 wavelengths) as it rotates about a vertical axis above a horizontal, buried wire (L = 0.152 wavelengths) (14) whose center is on the same vertical axis with a ground of $\epsilon_E = 9$ and $\sigma_{IG} = 0$ for a frequency of 1 MHz. When the wires are orthogonal, there is no interaction while the maximum effect is produced when they are parallel.

nuity at the junctions between segments, so that the final number is N_s.

The behavior of a numerical model, as N_s is increased, is often examined in what is called a "convergence test." Although a convergence test is reassuring if the numerical results approach an asymptote, it is not guaranteed that convergence takes place, or if it does, that the convergence is to the correct answer. In addition, depending on how results of the convergence test are examined, quite different conclusions might be reached, as demonstrated in Fig. 10.

The Time Domain

A similar approach is used to solve the time-domain version of the EFIE, Eq. (25), which is first written in operator form as (31,33)

$$O(s,t;s',t')F(s',t') = G(s,t) \tag{32a}$$

where t' is used here to denote the retarded time, that is $t' = t - R/c_\infty$. Then we might represent the space and time dependence of $F(s',t')$ as

$$F(s',t') = \sum_{i=1}^{N_s}\sum_{j=1}^{N_t} A_{ij}P_{ij}(s',t') \tag{33a}$$

where the A_{ij} are space-time samples of the unknown (i is the space index and j the time index) of which there are N_s and N_t space and time samples, respectively, so that Eq. (27) becomes

$$\sum_{i=1}^{N_s}\sum_{j=1}^{N_t} A_{ij}O(s,t;s',t')P_{ij}(s',t') = G(s,t) \tag{32b}$$

Upon sampling the field with the testing functions

$$\{W_{km}(s,t)\} = \{w_k(s)v_m(t)\}, k = 1,\ldots,N_s, m = 1,\ldots,N_t \tag{33b}$$

the operator equation is written in a discretized, sampled approximation as

$$\sum_{i=1}^{N_s}\sum_{j=1}^{N_t} A_{ij}\langle v_m(t), \langle w_k(s), O(s,t';s',t')P_{ij}(s',t')\rangle\rangle = \langle v_m(t), \langle w_k(s), G(s,t)\rangle\rangle \tag{32c}$$

where the inner product now involves a space integration and also a time integration.

Employing subsectional collocation in both space and time, the unknown current is written as

$$\begin{aligned} P_{ij}(s',t') =& A_{1,ij} + A_{2,ij}(s'-s_i) + A_{3,ij}(s'-s_i)^2 + A_{4,ij}(t'-t_j) \\ &+ A_{5,ij}(t'-t_j)^2 + A_{6,ij}(s'-s_i)(t'-t_j) \\ &+ A_{7,ij}(s'-s_i)^2(t'-t_j) + A_{8,ij}(s'-s_i)^2(t'-t_j)^2 \\ &+ A_{9,ij}(s'-s_i)^2(t'-t_j)^2, \\ & s_i - \Delta_i/2 \le s' < s_i + \Delta_i/2, i = 1,\ldots,N_s; \\ & t_j - \delta/2 \le t' \le t_j + \delta/2, j = 1,\ldots,N_t \end{aligned} \tag{34a}$$

and the constant time step is δ, whereas while the testing function is given by

$$W_{km}(s,t) = \delta(s-s_j)\delta(t-t_j) \tag{34b}$$

so that the tangential field is point-sampled in both space and time, and the time solution is developed from time stepping. There are nine unknown coefficients associated with each space-time step, eight of which are eliminated in a fashion similar to that described for NEC, by matching the current to

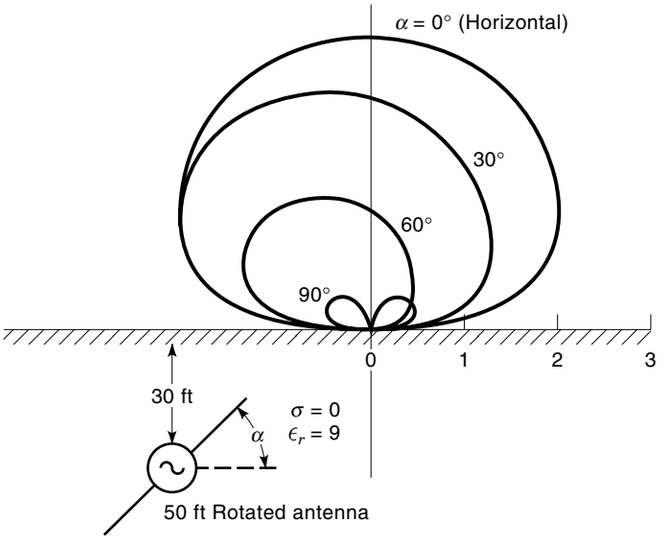

Figure 29. The TCA is used here to determine the above-ground radiation pattern of a dipole antenna as it rotates in a vertical plane (14). When the antenna is vertical or horizontal, the above-ground patterns are symmetric about a surface normal, but the patterns are otherwise slightly skewed.

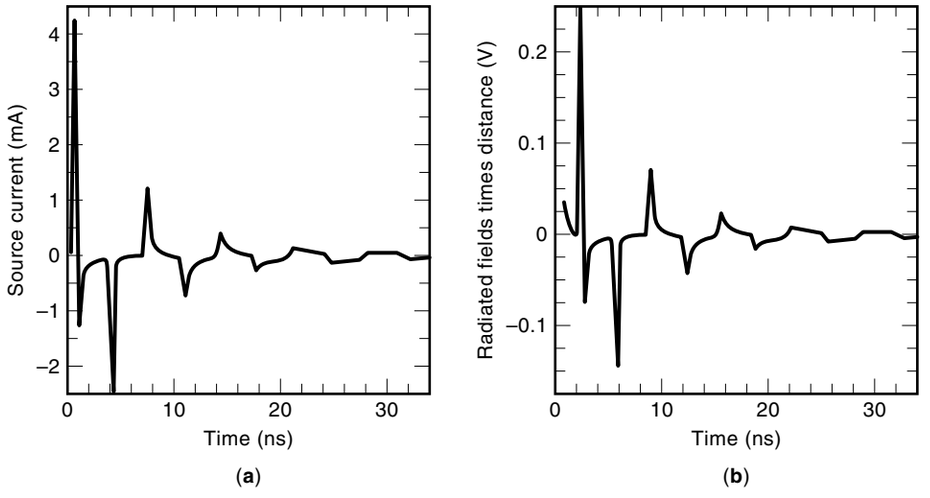

Figure 30. The source current (a) and the broadside electric field (b) for a dipole excited at its center by a Gaussian voltage as obtained using TWTD are quite similar, with the latter demonstrating the radiation for these conditions is first produced as the voltage is applied and then subsequently as the current–charge wave reflects from the wire ends (31).

its neighbors in the adjacent eight space-time samples (31,33) at $i \pm 1, j$; $i, j \pm 1$; $i \pm j, j \pm i$. An alternative approach is to write the basis function as $P_{ij}(s', t') = R_i(s')S_j(t')$, which then involves five unknowns (by setting the constant term in $S_j(t')$ to unity) and four are eliminated by matching at $i \pm 1, j$; $i, j \pm 1$. Finally, the space-time current samples are written in the form

$$I_{ij} = I(s_i, t_j) = Y_{ik}E^t_{kj} = Y_{ik}(E^i_{kj} + E^s_{kj}) = Y_{ik}\left[E^t_{kj} + \sum_{i'=1}^{N_s} Z_{ii'}I_{i',m-f(i,i')}\right] \tag{35}$$

where E^t_{ij} = total E_{ij}, E^s_{ij} = scattered E_{ij}.

For a straight wire, $f(i,i') = |i - i'|$, but it is generally a more complicated function of object geometry. Also, Y_{ik} represents the inverse of the time-independent matrix that accounts for field-current interactions in the time step j, and Z_{ii}, accounts for the fields produced over the object from currents that occurred at earlier times. Developed in this way, the time-stepping model is called "implicit," whereas if no interactions are allowed within time-step j, the model is "explicit." An example of a time-domain solution for a straight wire excited by a Gaussian voltage pulse, $V = V_0\exp(-t^2a^2)$, is given in Fig. 11, where the spatial distribution of current and charge are plotted at several instants of time (31).

Some Observations Concerning Numerical Modeling

Numerical models based on integral equations, like those presented in previously and solved by the moment method, as described previously, yield the source distribution, typically current for a wire antenna, for an arbitrary right-hand-side or incident field. All other observables of interest to the antenna designer or user are subsequently determined from this solution.

The code, or model, user usually devotes most attention to input impedance, radiation efficiency, and the directive gain or other antenna properties judged most important for the intended application. The model developer, on the other hand, is usually at least as interested in the current distribution, the convergent behavior of the numerical result revealed by its dependence on N_s, the near fields, and so on. For both the code user and code developer, validation of the code and the results obtained from it are crucially important. Validation ultimately consumes more time in computational electromag-

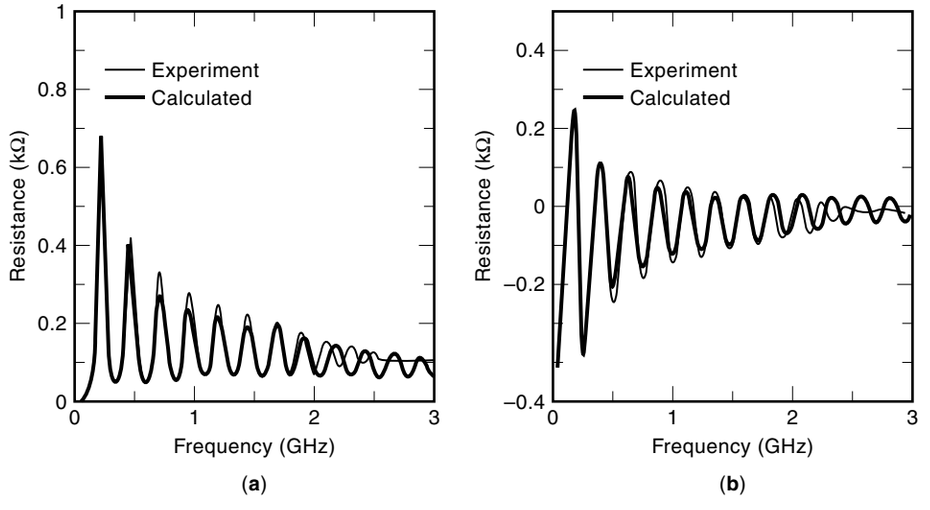

Figure 31. This comparison of the measured and computed, using TWTD, input impedance of a Gaussian-pulse excited antenna shows the two results are graphically indistinguishable for about the first 8 resonances (31), providing mutual validation, as well as demonstrating the broadband capability of a time-domain computation and measurement.

netics than any other single activity, but a discussion of it goes beyond the scope of this article. Some examples selected to exhibit the relative validity of numerical results are presented later, and further information about validation is found elsewhere (34).

The results presented later are selected from two perspectives. Aside from those chosen for explicit validation, one is to demonstrate some of the kinds of capabilities that wire models provide, primarily through results generated from NEC and TWTD. The other is to show the kinds of agreement expected between computation and measurement or other independent results.

SOME REPRESENTATIVE RESULTS OF WIRE-ANTENNA MODELING

Validating the Numerical Model

There are few analytical solutions for wire objects that validate a computer model, one exception being the well-known two-wire transmission line. A comparison of the results provided by an earlier version of NEC with those from analytical formulas is shown in Fig. 12 (16). For small antennas, there are also simple, analytical formulas for the input admittance (35), one of which used for an antenna in a plasma to check the results from NEC for a wire antenna in a lossy medium is shown in Fig. 13. In both cases, the IE model agrees with the analytical results to within a few percent.

Several different numerical models were used to determine the frequency response of a Vee-dipole, an antenna with V-shaped end loads connected by a short, straight center section where the antenna is excited (16). These model results, compared with each other over the frequency of the first resonance in Fig. 14, generally agree within 10%.

To be useful, wire codes must also model objects with fine detail, such as the zigzag shown in Fig. 15 (16). The first resonance of a constant-length zigzag is shown as a function of the angle between the adjacent one-inch segments, for which the measured and computed resonances agree within 5%.

A different kind of validation test is demonstrated in Fig. 16 where the input impedance of a dipole is presented as a function of distance from the interface between free space and a dielectric half-space (17).

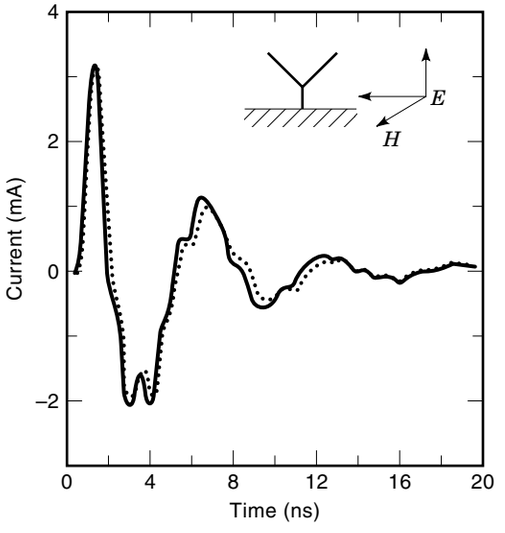

Figure 32. This comparison of the measured center current on a Vee-dipole due to a broadside-incident Gaussian plane wave with a TWTD prediction provides a mutual validation for both (31). The time displacement is evidently due to a slight time-scale difference.

Infinite-Medium Applications

Wire codes are typically used to determine input impedance, current distribution and radiation patterns of candidate antennas, but are also used for a variety of other applications. Some examples of these applications are shown here. In Fig. 17, the current distributions on a log-conical spiral antenna obtained from two different codes are compared. They agree within 10% relative to the peak values except right at the source (16). The radial component of the near field of a loop antenna is compared with independent data in Fig. 18. In Fig. 19, the input impedance of a loaded loop antenna is compared with measurement (16). A comparison of the measured and computed radiation patterns of a log-periodic dipole array antenna with foreshortened elements to reduce its physical size is presented in Fig. 20 (16). Finally, the frequency-dependence of the input impedance of a dipole antenna is illustrated in Fig. 21 for what are termed implicit and explicit source models (16). All of these results demonstrate the applicability of wire codes to various kinds of antennas for obtaining various observables.

Interface Applications

Because the "segmentation" or description of a continuous wire object using a piecewise linear approximation is not easily visualizable, a computer model of the Sectionalized-Loran Transmitting (SLT where LORAN stands for long range navigation) antenna is presented in Fig. 22 (28). The segments that comprise the numerical model are shown by arrows, where the reference direction for the current is in the direction to which the arrow points. This model contains 237 segments, or unknowns, a rather small number by today's standards where problems with thousands of unknowns are routinely modeled. This particular antenna was modeled over an imperfect ground with a radial-wire ground screen centered at the antenna feedpoint, using the combined RCA-ground-screen approach outlined previously.

Because a ground screen for an antenna this large requires a large amount of copper wire, it is desirable to use no more than necessary to achieve the desired performance characteristics. Therefore, parametric experiments were performed to determine the SLT's impedance sensitivity to its ground screen and the ground parameters, an example of which is shown in Fig. 23 (28).

One difficulty with modeling antennas located on or near the ground is validating the results of computer experiments, such as illustrated in Fig. 23. Fortunately, the U.S. Coast Guard, which operates the LORAN system obtained experimental measurements using a 1/25th scale-model antenna with 120 radials and with $\epsilon_{IG} = 15$, $\sigma_{IG} = 2 \times 10^{-2}$ S, for which some results are compared with computer predictions in Fig. 24 (28).

Two rather different kinds of interface modeling are presented next in Figs. 25 and 26. The effect on the input impedance of a vertical monopole antenna excited just above the

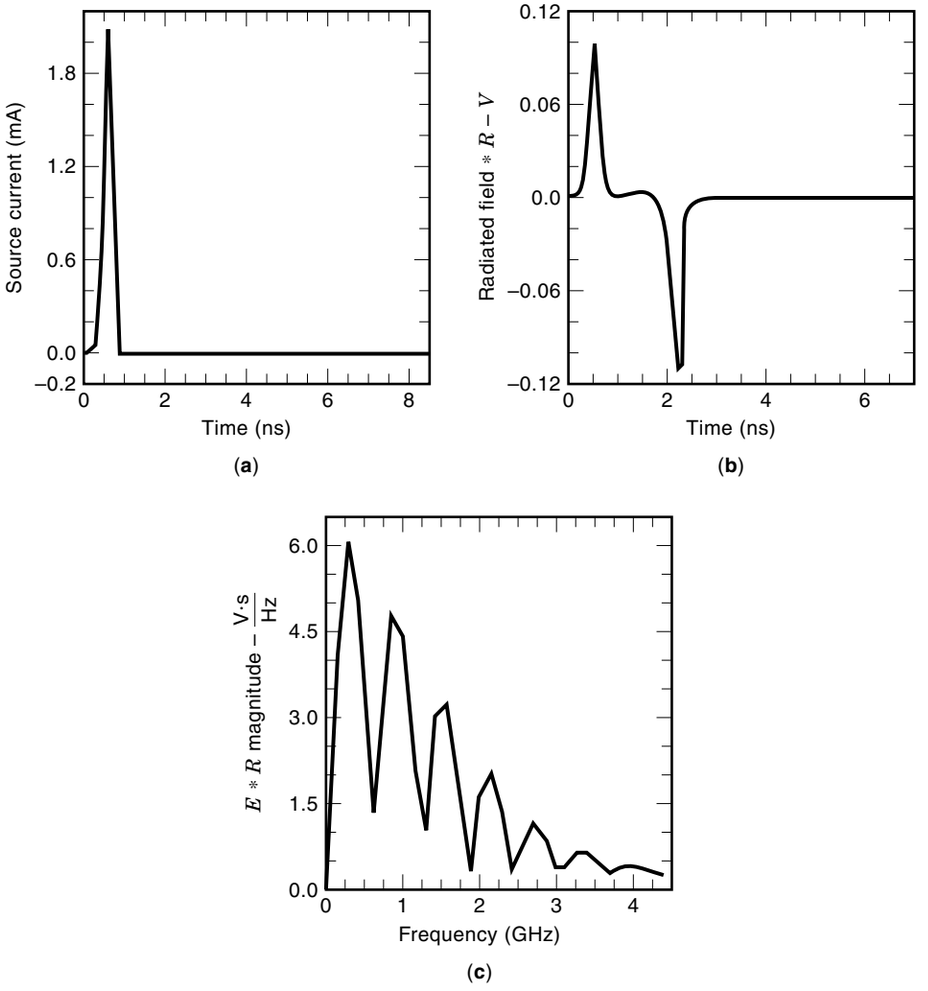

Figure 33. Nonlinear problems can be modeled in the time domain, as this result demonstrates. A dipole antenna continuously loaded with diodes that permit it to conduct in only one direction has the feedpoint current in (a), and broadside radiated field in (b) when excited by a Gaussian pulse (31). The spectrum of the radiated field is as shown in (c).

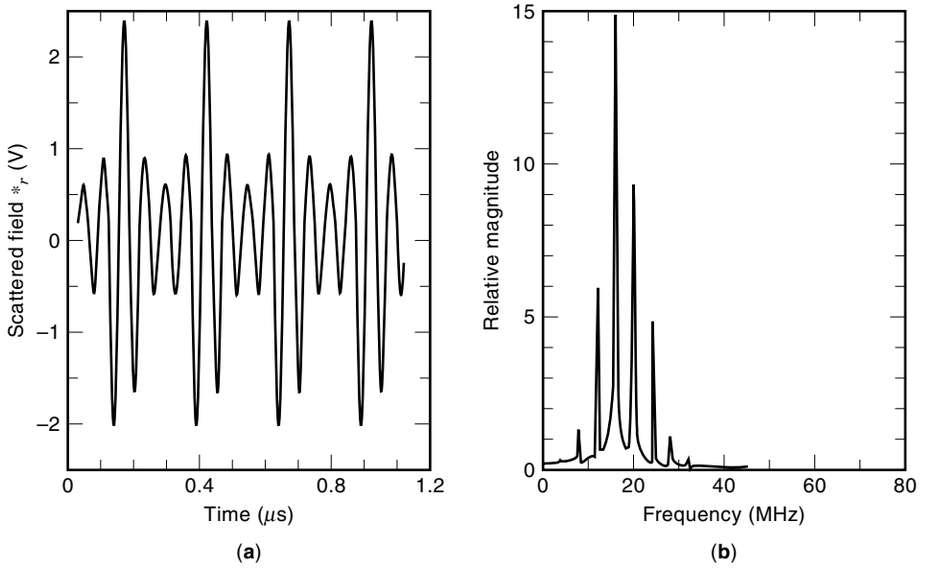

Figure 34. Time varying problems are also well-suited to time-domain modeling as demonstrated here (31). A 16 MHz, broadside-incident, plane wave illuminates a half-wave diople having a center load whose resistance varies sinusoidally at 4 MHz, producing the broadside scattered field in (a) whose spectrum is shown in (b). Dynamically varying the reflectivity of a scatterer can be used to change the scattered-field spectrum from what it otherwise would be.

interface on the length of the buried ground stake against which it is driven is illustrated in Fig. 25 (24). The dependence of the radiation pattern of a monopole antenna driven against a ground screen which consists of only a few radial wires just above the surface of the ground is demonstrated in Fig. 26. These kinds of problems are ideally suited for computer analysis and parametric optimization, because developing such data experimentally is generally impractical.

The modeling of buried objects and antennas is illustrated in Figs. 27–29. The normalized impedance change of a horizontal dipole in the upper air medium plotted versus its distance from a vertical plane containing a buried, horizontal wire to which it is parallel is shown in Fig. 27. These results were obtained by the Sommerfeld theory outlined previously and the Transmission-Coefficient Approximation (TCA), an extension of the RCA described previously to the computation of fields on the other side of an interface from the source (13). In Fig. 28, the effect on its input impedance of rotating an upper-medium, horizontal-dipole antenna relative to a buried wire is demonstrated, also obtained by the TCA. Finally, the radiation pattern of a buried antenna is presented for several different rotational angles relative to the interface normal in Fig. 29.

Time-Domain Applications

There are several advantages in performing time-domain modeling. One advantage is that wideband data are available from one model computation as opposed to the many frequency samples required to obtain equivalent data from a frequency-domain code. Another advantage is a more straightforward approach to modeling impedance nonlinearities in the time domain. A third advantage is that time-domain models also handle time variations in load impedances. An example of the first is illustrated in Fig. 30 (31), where the transient feedpoint current and broadside radiated field are shown for a Gaussian-pulse-excited dipole. Upon Fourier transforming the feedpoint current, the input impedance is obtained across a wide bandwidth, as presented in Fig. 31 (31). The measured current at the center of a Vee-dipole antenna excited by a Gaussian plane-wave incident pulse is presented in Fig. 32 and compared with a TWTD computation, where the amplitudes of the two results agree to within a few percent but a slight difference in the time axis is seen.

Use of a time-domain model for nonlinear loading is demonstrated in Fig. 33 where the input current, broadside radiated field and the radiated-field spectrum are presented, as computed from TWTD. The radiated field has two opposite-sign pulses, caused by the initial turn on of the drive voltage and the stopping of the current-charge pulses as their outward propagation is stopped. When a dipole is illuminated by a time-harmonic plane wave incident from broadside while its center load varies sinusoidally in value, the results of Fig. 34 are obtained. Interaction of the incident field and the time-varying load causes intermodulation products that produce upper and lower sidebands in the scattered field.

BIBLIOGRAPHY

1. A. J. Poggio and E. K. Miller, Low-frequency analytical and numerical methods for antennas. In Y. T. Lo and S. W. Lee, eds., *Antenna Handbook,* New York: Van Nostrand Reinhold, 1988, pp. 3-1 to 3-98.
2. G. J. Burke, *Numerical Electromagnetics Code—NEC-4 Method of Moments, Part II: Program Description—Theory.* Lawrence Livermore National Laboratory, Rept. USRL-MA-109338, January 1992.
3. J. A. Landt, E. K. Miller, and M. L. Van Blaricum, *WT-MBA,LL1B: A Computer Program for the Time Domain Analysis of Thin-Wire Structures,* Livermore, CA: Lawrence Livermore Laboratory, UCRL-52172, 1976.
4. A. J. Poggio and E. K. Miller, Integral-equation solutions of three-dimensional scattering problems. In *Computer Techniques for Electromagnetics,* New York: Pergamon Press, 1973, pp. 159–264.
5. R. M. Bevensee, *Design Considerations for Parasitic Screen Antennas.* Lawrence Livermore Laboratory Report, Rept. UCID-16657, 1975.
6. E. K. Miller, A selective survey of computational electromagnetics, invited tutorial-review paper. *IEEE Trans. Antennas Propag.* **AP-36**:, 1281–1305, 1988.
7. E. S. Selden and G. J. Burke, *DLGN-38 Final Report.* MBAssociates, San Ramon, CA, Tech. Rept. MB-R-75/16, 1975.
8. D. L. Jaggard, On bounding the equivalent radius. *IEEE Trans. Antennas Propag.,* **AP-28**: 384–388, 1980.
9. O. M. Salati, Antenna chart for system designers. *Electron. Eng.,* January 1968.
10. E. K. Miller et al., Analysis of wire antennas in the presence of a conducting half-space. Part I: The vertical antenna in free space. *Canadian J. Physics,* **50**: 879–888; Part II: The horizontal antenna in free space, *Canadian J. Physics,* **50**: 2614–2627, 1971.
11. A. Sommerfeld, *Partial Differential Equations in Physics.* New York: Academic Press, 1964.
12. G. J. Burke and E. K. Miller, Modeling antennas near to and penetrating a lossy interface. *IEEE Trans. Antennas Propag.* **AP-32**: 1040–1049, 1984.
13. A. Banos, *Dipole Radiation in the Presence of a Conducting Half-Space.* New York: Pergamon Press, 1966.
14. E. K. Miller and F. J. Deadrick, *Analysis of Wire Antennas in the Presence of a Conducting Half Space: Part III—The Buried Antenna.* Lawrence Livermore Laboratory, Rept. UCRL-52228, January 1977.
15. I. V. Lindell, E. Alanen, and K. Mannersalo, Exact image theory for computation of antennas above the ground. *IEEE Trans. Antennas Propag.* **AP-33**: 937–945, 1985.
16. E. K. Miller, Wires and wire-grid models for radiation and scattering including ground effects. In *Theoretical Methods for Determining the Interaction of Electromagnetic Waves with Structures,* Rockville, MD: Sijthoff and Noordhoff, 1981, pp. 57–95.
17. G. J. Burke, E. K. Miller, J. N. Brittingham, D. L. Lager, and R. J. Lytle, Computer modeling of antennas near the ground. *Electromagnetics,* **1**: 29–49, 1981.
18. E. K. Miller, J. N. Brittingham, and J. T. Okada, Bivariate-interpolation approach for efficiently and accurately modeling antennas near a half-space. *Electronics Letters,* **13**: 690–691, 1977.
19. E. S. Cassidy and J. Fainberg, Back scattering cross sections of cylindrical wires of finite conductivity. *IRE Trans. Antennas Propag.,* **AP-8**: 1, 1960.
20. J. H. Richmond, *Radiation and Scattering by Thin-Wire Structures in the Complex-Frequency Domain,* Columbus, OH: Ohio State U., Electro Science Lab., Rept. 2902-10, 1973.
21. R. W. P. King and G. S. Smith, *Antennas in Matter.* Cambridge, MA: The MIT Press, 1981.

22. R. W. P. King et al., The insulated monopole: Admittance and junction effects. *IEEE Trans. Antennas Propag.,* **AP-23**: pp. 172–177, 1975
23. J. R. Wait, Characteristics of antennas over lossy earth. In R. E. Collin and F. J. Zucker, eds., *Antenna Theory.* New York: McGraw–Hill, 1969, pp. 286–437.
24. E. K. Miller, Numerical modeling techniques for antennas. *NATO AGARD Lecture Series No. 131,* NASA, Langley Field, VA, 1983, pp. 7-1 to 7-29.
25. G. J. Burke, Recent advances to NEC: Applications and validation. *NATO AGARD Lecture Series No. 165,* NASA, Langley Field, VA, 1989, pp. 3-1 to 3-35.
26. J. R. Wait and W. A. Pope, The characteristics of a vertical antenna with a radial conductor ground system. *Appl. Sci. Res.,* Sec. B, **4**: 177–195, 1954.
27. J. R. Wait, *Electromagnetic Waves in Stratified Media.* New York: Pergamon Press, MacMillan Co., 1962.
28. E. K. Miller and F. J. Deadrick, *Computer Evaluation of LORAN-C Antennas,* Livermore, CA: Lawrence Livermore National Laboratory, Rept. UCRL-51464, 1973.
29. G. A. Thiele and P. Tulyathan, A hybrid technique for combining moment methods with the geometrical theory of diffraction. *IEEE Trans. Antennas Propag.* **AP-26**: 587–592, 1978.
30. X. Yuan, R. D. Lynch, and J. W. Strohbehn, Coupling of finite element and moment methods for electromagnetic scattering from inhomogeneous objects. *IEEE Trans. Antennas Propag.,* **AP-38**: 386–393, 1990.
31. E. K. Miller and J. A. Landt, Direct time-domain techniques for transient radiation and scattering from wires, invited paper. In *Proc. IEEE,* **68**: 1396–1423, 1980.
32. R. F. Harrington, *Field Computation by Moment Methods.* New York: MacMillan, 1968.
33. R. G. Martin, A. Salinas, and A. R. Bretones, Time-domain integral equations methods for transient analysis. *IEEE Antennas Propag. Mag,* **34**(3): 15–22, 1992.
34. E. K. Miller, Characterization, comparison, and validation of electromagnetic modeling software. *ACES J.,* special issue on Electromagnetics Computer Code Validation, **4**: 8–24, 1989.
35. K. G. Balmain, Dipole admittance for magnetoplasma diagnostics. *IEEE Trans. Antennas Propag.,* **AP-17**: 389–392, 1969.
36. Y. S. Yeh and K. K. Mei, Theory of conical equiangular spiral antennas: Part I. Numerical techniques. *IEEE Antennas Propag.,* **AP-15**: 634–639, 1967.
37. R. L. Fante, J. J. Otazo, and J. T. Mayhan, The near field of the loop antenna. *Radio Sci.,* **4**: 697, 1969.
38. E. K. Miller, J. N. Brittingham, and J. T. Okada, Explicit modeling of antennas with sparse ground screens. *Electron. Lett.,* **14**: 627–629, 1978.

EDMUND K. MILLER